

Investigation on the Dynamic Rupture of the 1970 M_s 7.7 Tonghai, Yunnan, China, Earthquake on the Qujiang Fault

Houyun Yu¹, Wenqiang Zhang¹, Zhenguo Zhang^{*2}, Zhengbo Li¹, and Xiaofei Chen²

ABSTRACT

Regional stress states and fault geometries play important roles in earthquake rupture dynamics. Using the curved grid finite-difference method, we conducted 3D spontaneous rupture simulations of the nonplanar Qujiang fault (QF) to investigate the rupture processes of the 1970 Tonghai earthquake and potential future earthquakes. A nonplanar fault model including topography was adopted and embedded in heterogeneous media. Regional stress orientations with an interval of 5° were tested, and various fault geometry models with different fault surface traces and fault dips were discussed. We also provided explanations for the unbroken northwestern segment of the QF and the seismic intensity anomaly in the Tonghai basin during the 1970 Tonghai event. Finally, we presented several future potential earthquake scenarios occurring on the QF at three nucleation locations. Our simulation results suggested that the maximum principal stress azimuth around the Tonghai area is $N25^\circ W$ and that the QF is most likely a complex dipping fault—the southeastern segment dips to the northeast, whereas the northwestern segment dips to the southwest. Our simulations also revealed that multiple explanations, including a regional stress rotation and an increase in the cohesion force, could account for the unbroken northwestern segment of the QF. Furthermore, the seismic intensity anomaly in the Tonghai basin can be explained by a low-velocity structure. Future earthquake scenarios demonstrated that potential earthquakes nucleating at Eshan and Wujie in a complex dipping fault model could rupture the entire QF, thereby posing severe seismic risks to nearby regions. In contrast, when the nucleation point was located at Quxi, the rupture was constrained to the initial fault segment of the QF; however, caution should still be exercised in the Quxi area because this scenario produces a maximum intensity of VIII.

KEY POINTS

- We model the dynamic rupture and strong ground motion of the 1970 M_s 7.7 Tonghai, China, earthquake.
- The models support several explanations for the rupture stopping at the northwest segment of the fault.
- The results show the roles that fault geometry, stress field, and velocity structure have on ground motions.

Supplemental Material

INTRODUCTION

Unlike the 1975 M_s 7.3 Haicheng earthquake preceded by a rich set of precursors (Chen *et al.*, 1975; Yang, 1982) and the 1976 M_s 7.8 Tangshan earthquake accompanied by aggravated damage (Guo *et al.*, 1977; Chen *et al.*, 1979), the 1970 M_s 7.7 Tonghai earthquake (M_w 7.2, Yan *et al.*, 2018) during the same period in Yunnan, China, is not well understood by the scientific community and the public, even though this

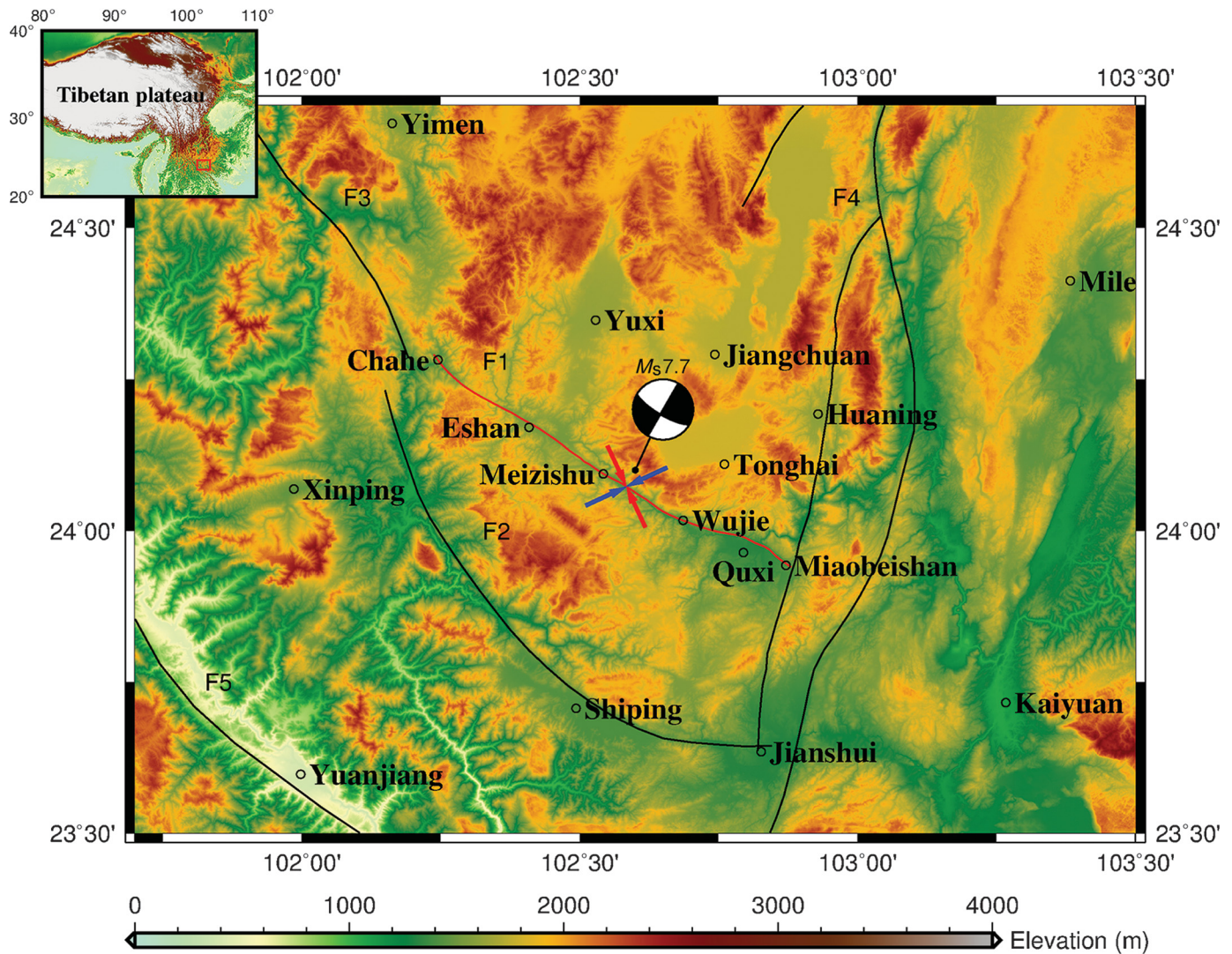
earthquake killed more than 15,000 people. This earthquake occurred on the Qujiang fault (QF). Some observed phenomena surrounding this earthquake are scientifically interesting, such as the northwestern QF segment remaining unbroken and the intensity anomaly in the Tonghai basin (Zhang and Liu, 1978; Liu *et al.*, 1999). This devastating event struck the southeastern tip of the Sichuan–Yunnan block, which is one of the most seismically active regions in China (Kan *et al.*, 1977; Wang *et al.*, 2014). This block is located along the southeastern margin of the Tibetan plateau and is bounded by the stable South China block to the east and the Indochina block to

1. School of Earth and Space Sciences, University of Science and Technology of China, Hefei, China; 2. Department of Earth and Space Sciences, Southern University of Science and Technology, Shenzhen, China

*Corresponding author: zhangzg@sustech.edu.cn

Cite this article as Yu, H., W. Zhang, Z. Zhang, Z. Li, and X. Chen (2020). Investigation on the Dynamic Rupture of the 1970 M_s 7.7 Tonghai, Yunnan, China, Earthquake on the Qujiang Fault, *Bull. Seismol. Soc. Am.* **110**, 898–919, doi: 10.1785/0120190185

© Seismological Society of America



the west. Accordingly, as a result of the extrusion of the Tibetan plateau motivated by the northward collision of the Indian plate with the Eurasian plate, the Sichuan–Yunnan block exhibits movement toward the southeast (SE) (Tapponnier *et al.*, 1982; Deng *et al.*, 2002; Wen *et al.*, 2011).

The epicenter of the Tonghai earthquake, which occurred on 5 January 1970, was located at 102.6° E and 24.1° N, close to Meizishu (Fig. 1), and the focal depth was about 13 km (Zhang and Liu, 1978). The surface rupture related to this event stretched over 48 km, and the corresponding surface displacements are well documented (Zhang and Liu, 1978; Liu *et al.*, 1999). Figure 1 illustrates the surface trace of the seismogenic fault of this event, the earthquake rupture of which was dominated by dextral strike-slip movements with a maximum strike-slip displacement of 3.25 m (Liu *et al.*, 1999). The source process characteristics of the Tonghai earthquake suggest a bilateral rupture and indicate that the seismic energy during this event was concentrated mainly in the southeastern extent of the research area (Zhang and Liu, 1982; Zhou *et al.*, 1983). The event affected most of the Yuxi region, which is famous throughout China for growing tobacco.

Figure 1. Map view of the Qujiang fault (QF, F1), which is modified from Zhu (1985) and Wang *et al.* (2014), as indicated by the red line. The focal mechanism of the 1970 Tonghai earthquake is from Zhou *et al.* (1983). The blue and red arrows illustrate the preferred directions of the maximum and minimum horizontal principal compressive stresses, respectively. The black lines show the neighboring faults: F2 for the Shiping–Jianshui fault, F3 for the Chuxiong fault, F4 for the Xiaojiang fault, and F5 for the Red River fault. The background colors reflect the surface topography. The inset in the upper left corner shows the position of the research area relative to the Tibetan plateau.

A map of the documented intensity of this earthquake shows a nearly symmetric elliptical intensity distribution. The event produced a maximum intensity of X on the Chinese seismic intensity scale (Fig. 2). The Chinese seismic intensity scale is listed in Table 1 (Sun *et al.*, 2008). The documented intensity (Liu *et al.*, 1999) presented in Figure 2 also shows an intensity anomaly in the Tonghai basin, where the seismic intensity distribution is characterized by a IX-intensity area surrounded by a VIII-intensity region. The Tonghai basin is located northeast (NE) of the epicenter of the Tonghai event. It has a length of

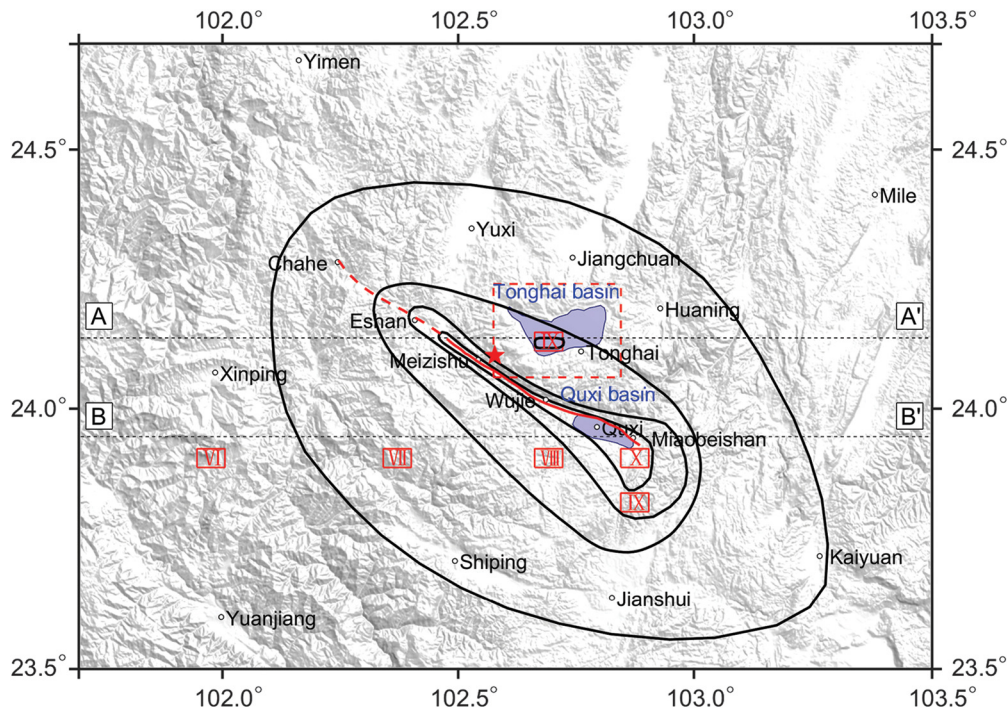


Figure 2. Documented intensity distribution of the 1970 Tonghai earthquake from Liu *et al.* (1999), with the intensities indicated in bold black contour lines and red Roman numerals with red rectangles. The red solid line illustrates the surface rupture of the QF during the 1970 Tonghai earthquake, whereas the red dashed line represents the unbroken northwestern QF segment (Zhang and Liu, 1978). Two dashed black lines, AA' and BB', represent two profiles illustrating the velocity structure. The velocity profiles are shown in Figure 4. The two blue shaded areas denote the shapes of the Tonghai basin and the Quxi basin modified from He *et al.* (2013) and Wang *et al.* (2014), respectively. The red dashed rectangle emphasizes the Tonghai area and will be used in The low-velocity basin effect section.

nearly 20 km and a width of 10 km, and the deepest sedimentary depth is approximately 450 m (He *et al.*, 2013). Another basin that is close to the QF is the Quxi basin. The Quxi basin is smaller than the Tonghai basin, at approximately 15 km long and 5 km wide, and it lies at the southeastern end of the QF. However, the Quxi basin has a deeper sedimentary depth, reaching 700 m below the free surface (Wang *et al.*, 2014). Although the Tonghai basin and the Quxi basin are small compared with the whole research area (blue-shaded area in Fig. 2), many investigations have shown that low-velocity structures are of great importance to strong ground motions (Semblat *et al.*, 2005; Ewald *et al.*, 2006; Duan, 2008; Chaljub *et al.*, 2015; Zhang *et al.*, 2017; Rodgers *et al.*, 2019).

A geological survey performed after the Tonghai event did not reveal a surface rupture west of Eshan (Zhang and Liu, 1978). The damage distribution also suggests that the northwestern segment of the QF remained unbroken during the devastating event (Fig. 2). Now we may ponder the following question: why did the rupture of the Tonghai event die out when it reached Eshan? Was the behavior caused by regional stress fields? Although no focal mechanisms indicating the stress orientation that have been resolved on the northwestern

QF are different from those resolved on the southeastern QF, Global Positioning System (GPS) data have shown that the displacement directions near the northwestern part of the QF point to the south and SW (Wei *et al.*, 2012; Liu *et al.*, 2016), and the movement direction of the crust reflects the stress orientation to some extent. Alternatively, some research has indicated that an earthquake could also cause a rotation of the regional stress orientation, with the rotation even reaching 30° (Yamashita *et al.*, 2004; Duan, 2010; Yoshida *et al.*, 2016). Moreover, we noted that, in 1913, an M 7.0 earthquake that caused a maximum intensity of VIII in Eshan ruptured most of the northwestern segment of the QF (Zhu, 1984; Liu *et al.*, 1999; Wen *et al.*, 2011). Therefore, the stress orientation near Eshan may have been rotated after the 1913 M 7.0 earthquake. Was this caused by the changing of fault-plane properties due to

the aforementioned earthquake? Once an earthquake occurs, the rock properties and fault-plane coefficients, such as the cohesive force on the fault plane (Muhuri *et al.*, 2003), can change considerably. As indicated by Tenthoery and Cox (2006), the cohesive force on a fault plane of sandstone in the laboratory could increase by as much as 35 MPa after only 6 hr under specific temperature and pressure conditions.

Was this phenomenon caused by the QF geometry, such as stepovers or faults with part of the segment missing, because there is no visible surface trace of the QF that can be tracked near Eshan (Zhu, 1985; Wang *et al.*, 2014)? As presented in Figures 1 and 2, the QF has been identified as the seismogenic fault that produced the Tonghai earthquake. The total length of the QF is approximately 80 km, with a general strike of N60°W. Its strike changes to nearly east–west at Wujie, beyond which it forms a restraining bend and then reverts to its previous strike (Fig. 1). Field investigations revealed that the QF surface trace, from which we construct the fault geometry model, is not a single continuous fault; instead, it consists of many fault segments and may be characterized by particular fault combinations such as branched and stepover faults (Zhu, 1984, 1985; Wang *et al.*, 2014). By comparing the surface rupture from

TABLE 1

Chinese Seismic Intensity Scale

Parameter	I	II	III	IV	V	VI	VII	VIII	IX	X
PGA _h (m/s ²)	–	–	–	–	0.31	0.63	1.25	2.50	5.00	10.00
PGV _h (m/s)	–	–	–	–	0.03	0.06	0.13	0.25	0.50	1.00

PGA_h, horizontal component of the peak ground acceleration; PGV_h, horizontal component of the peak ground velocity.

Zhang and Liu (1978) with the field investigations from Zhu (1985) and Wang *et al.* (2014), we may identify two possible stepovers along the QF—one is located at Eshan, and the other is located Wujie. A complex fault geometry, including stepovers, could have significant influences on the results of dynamic rupture and wave propagation simulations (Aochi and Fukuyama, 2002; Aochi and Madariaga, 2003; Kase and Day, 2006; Aochi and Kato, 2010; Oglesby and Mai, 2012; Douilly *et al.*, 2015; Zhang *et al.*, 2017; Hu *et al.*, 2018; Rodgers *et al.*, 2019).

At the same time, the dip of the QF is poorly understood, and different studies have revealed that the dip of the QF can be very complex, ranging from 45° NE to 60° southwest (SW). Field investigations showed that most of the QF segments dip toward the NE at a high angle, and some are even vertical (Zhang and Liu, 1978; Zhu, 1985). The focal mechanism research of the Tonghai earthquake by Zhang (1980) similarly revealed that the seismogenic QF dips toward the NE with a dip angle of 80°. From the tectonic perspective, Wen *et al.* (2011) deduced that the QF dips toward the NE at an angle of 70°. However, the focal mechanism calculated from the *P*-wave first motions by Zhang and Liu (1982) showed that the fault-plane dips toward the SW with a nearly vertical dip angle of 85.8°. Using the ground deformation data, Wang *et al.* (1978) inverted the fault parameters of the Tonghai event and illustrated that the QF dips toward the SW at an angle of 84°. This perspective is also supported by the locations of aftershocks (Wang *et al.*, 1978; Zhang and Liu 1978; Liu *et al.*, 1999). Confusingly, some evidence obtained from field investigations has emphasized that the northwestern segment of the QF dips toward the SW and that the southeastern segment dips toward the NE (SW–NE), as shown in Zhu (1984, 1985) and Zhou *et al.* (1995), and they revealed that the dip inflection point is located near Eshan. Detailed field geological observations by Wang *et al.* (2014) revealed similar results, but they also suggested that the QF dips toward the NE at depth.

The Tonghai earthquake, which was a typical right-lateral strike-slip earthquake, was initiated along the QF. Various studies have been conducted to obtain a comprehensive understanding of the QF and the earthquake itself. Zhu (1985) discussed the Quaternary activity of the QF and constructed a detailed and convincing fault surface geometry based on a field investigation. Liu *et al.* (1999) indicated that the QF has been highly active since the Quaternary, and as a result,

four Holocene paleoearthquakes with magnitudes greater than *M* 7.0 have been detected. Studies on the QF and adjacent areas using GPS data have shown that the present-day QF is tectonically active, with a 4.5 mm/yr dextral strike-slip rate and a 2.5 mm/yr total crustal shortening rate (Wen *et al.*, 2011). Moreover, a thorough geological survey conducted by Wang *et al.* (2014) revealed a right-lateral slip rate along the QF of 2.84–3.27 mm/yr, as deduced from the topographic displacement since the late Pleistocene. For the Tonghai event, Wang *et al.* (1978) determined the seismogenic fault parameters of the QF using documented surface deformation data and obtained a planar fault model with an average fault slip of 2.24 m and a stress drop of 3.4 MPa along the fault plane. Recently, Tan *et al.* (2017) inverted these deformation data and obtained a slip distribution on the fault plane with a maximum slip of 3 m. Furthermore, Zhou *et al.* (1983) estimated the rupture process with *P*-wave data. Their results implied that the Tonghai earthquake exhibited a complex-source rupture process that potentially consisted of three to four subevents at different moments.

The Tonghai earthquake struck about 50 yr ago. Nevertheless, although many researchers have focused on the Tonghai earthquake and the QF, some problems remain unresolved. For example, what were the stress conditions during the Tonghai earthquake? In addition, why did the rupture of this event not propagate to the northwestern segment of the QF? In this study, we use a new method developed in recent years to conduct spontaneous rupture simulations of the 1970 Tonghai earthquake to investigate the rupture process of this event based on a nonplanar fault model with topography embedded in heterogeneous media. Here, we first investigate the regional stress orientations and discuss the effects of the fault geometry on the rupture dynamics of the Tonghai earthquake to find the best-matched rupture process model from a numerical simulation perspective. Then, we discuss why the northwestern segment of the QF did not rupture by comparing the recorded data with surface dislocations, ground deformation data, and the seismic intensity distribution derived from the numerical simulations. In addition, we investigate why an intensity anomaly was observed within the Tonghai basin. Finally, we perform dynamic rupture simulations of future potential earthquake scenarios along the QF using the previously obtained preferred fault models and stress states to provide a better understanding of the rupture process of the QF during

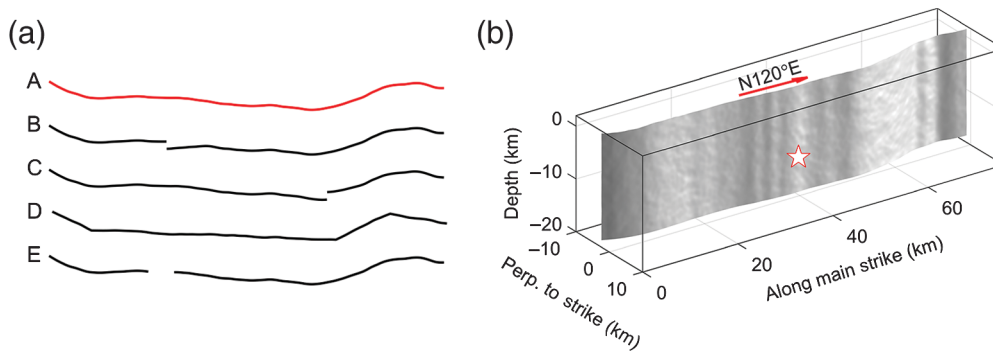


Figure 3. (a) Different fault surface trace geometries used in the numerical simulations. Traces A, B, C, and E were modified from Zhu (1985) and Wang *et al.* (2014), whereas trace D is simplified from trace A. (b) 3D view of the nonplanar fault geometry based on the fault surface geometry of trace A. The white star with the red edges denotes the hypocenter of the 1970 Tonghai event.

the Tonghai earthquake and to improve regional hazard assessments and risk prevention endeavors.

NUMERICAL METHOD AND MODEL CONSTRUCTION

Numerical method

There are many codes available for dynamic earthquake rupture and wave propagation simulations, such as EQdyna (Duan and Oglesby, 2006), PyLith (Aagaard *et al.*, 2013), SPECFEM3D (Galvez *et al.*, 2014), WaveQLab3D (Duru and Dunham, 2016), etc. Determining the method adopted for dynamic rupture modeling depends on the needs of the simulation. Here, we want to simulate the rupture process of the nonplanar QF during the Tonghai earthquake, considering the coupling of the topographical surface with heterogeneous subsurface media. The curved grid finite-difference method (CG-FDM) developed by Zhang and Chen (2006) and Zhang *et al.* (2014), which uses the collocated-grid finite-difference method with governing equations of first-order velocity–stress formulations for fault rupture propagation, allows complex fault geometries and irregular topography to be modeled and has been verified by benchmark models (Harris *et al.*, 2018). Hence, the CG-FDM is a good candidate for modeling the elements described earlier.

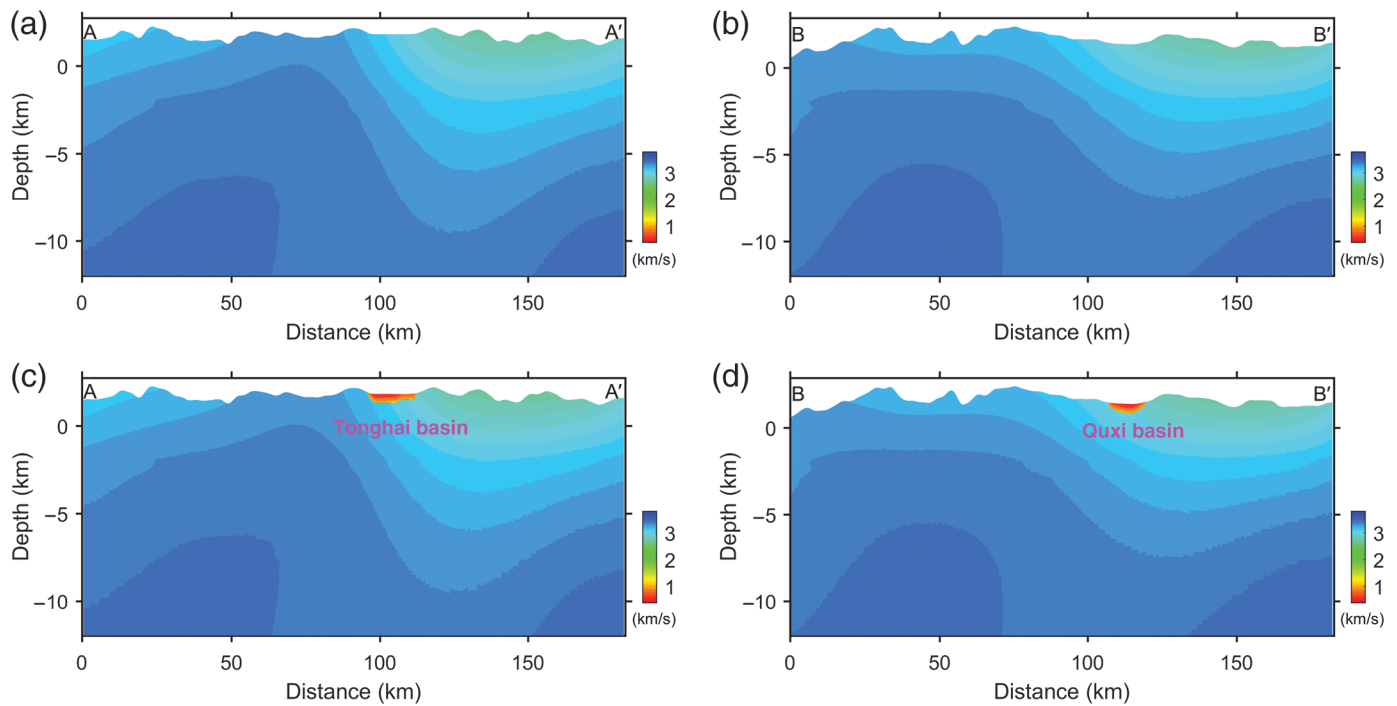
Fault geometry model

The surface geometry of the QF is derived mainly from field investigations (Zhu, 1984, 1985; Wang *et al.*, 2014), from which we constructed the 3D fault geometry model, which can be found in Figure 3a. We retained as many of the fault geometry details as possible when considering a single continuous fault with a general strike of N120°E (Fig. 3a). First, we adopted a vertical-dipping fault model based on fault trace A (Fig. 3a), as discussed in the Regional principal stress orientations section. Then, we constructed two vertical-dipping stepover fault geometry models based on surface trace models B and C in

Figure 3a with stepovers at Eshan and Wujie, both with a step distance of 1 km, to investigate the fault surface geometry effect. A simplified vertical fault model based on a four-segment fault surface trace model, trace D in Figure 3a, was also considered here because field investigations have not been performed for all faults. If a simplified fault geometry produces a dynamic rupture and ground-motion pattern similar to a complex curved fault, we can use the simplified geometry as a substitute for the complex fault geometry.

Moreover, three different dipping fault geometry models based on trace A (Fig. 3a) were also constructed to investigate the fault dipping effects in the Effects of the fault geometry section. The first fault geometry model dips toward the NE with a dip angle of 75°. The second dipping fault model dips toward the SW, and it also dips at an angle of 75°. The last QF geometry model is relatively complex, with the fault dipping toward the SW west of Eshan, whereas the remainder of the fault dips toward the NE (SW–NE). In this case, the fault plane at Eshan is vertical, that is, the dip angle is 90°, whereas the dip angles at the western and eastern ends of the QF are 80° and 75°, respectively, and dips anywhere else along the QF were obtained by linear interpolation. With fault surface trace E in Figure 3a, which has a 5 km fault gap near Eshan, we also constructed a complex dipping fault geometry model, and henceforth, we define this geometry model as the fault absence model, which will be used in the Unbroken northwestern segment of the QF section.

In all of the aforementioned fault models, the along-strike length of the fault model is 77 km, and the seismogenic fault width is 20 km, which were deduced from the locations of aftershocks (Zhang and Liu, 1978; Liu *et al.*, 1999). This means that the basal depth of the fault is deeper when the dip is closer to vertical. The fault model was constructed with the topography, which was interpolated from Shuttle Radar Topography Mission (SRTM) 90 m topography database (Jarvis *et al.*, 2008), because the ground surface topography can dramatically impact the rupture process and strong ground motion (Lee *et al.*, 2009; Zhang *et al.*, 2016; Huang *et al.*, 2018). Also, we already know that the roughness of the fault plane contributes to high-frequency seismic-wave radiation in dynamic rupture simulations (Andrews and Barall, 2011; Shi and Day, 2013). Thus, we applied a rough fault surface with Hurst exponents $H = 0.4$ and a roughness amplitude of 200 m in our fault geometry model (Andrews and Barall, 2011; Dunham *et al.*, 2011;



Shi and Day, 2013). The nonplanar fault model was discretized into 1540×400 grid points with an average grid spacing of 50 m. Figure 3b shows a 3D view of the vertical-dipping fault model based on fault trace A.

Velocity model

The dynamic rupture simulations were computed on a nonplanar fault model embedded in heterogeneous elastic media. Shen *et al.* (2016) presented a 3D V_S reference model of China with resolutions of 0.5° in the horizontal direction and 500 m in the depth direction. We used this velocity model to evaluate the V_S velocity of each grid on the fault plane and in other computational domains through linear interpolation. For the grids above sea level, we performed linear extrapolation to obtain the velocities. Using empirical relations between the elastic wavespeeds and density (Brocher, 2005), we obtained the corresponding V_P and density on each grid. We adopted this velocity model in the Regional principal stress orientations, the Effects of the fault geometry, and the Unbroken northwestern segment of the QF sections.

Moreover, as mentioned previously, the documented intensity map presented in Figure 2 shows an intensity anomaly in the Tonghai basin. We investigated this intensity anomaly phenomenon by adding two small basin structures to the velocity model. These two low-velocity structures of the Tonghai basin and the Quxi basin are modified from He *et al.* (2013) and Wang *et al.* (2014), respectively. The sedimentary basins are described in layers with a minimum V_S of 400 m/s at the basin surface. Figure 4 presents two V_S profiles, AA' and BB', shown in Figure 2 across the Tonghai basin and the Quxi basin. Figure 4a,b illustrates the V_S distributions from the

Figure 4. Distributions of V_S along two profiles, AA' and BB', which are plotted in Figure 2. Note that we plot to a depth of only 12 km, so the X and Y axes are not equal in scale. The velocities in (a) and (b) are interpolated from Shen *et al.* (2016). The profiles in (c) and (d) are the same as those in (a) and (b) but with two layered low-velocity basin structures.

interpolation of data from Shen *et al.* (2016). Figure 4c,d is the corresponding V_S distributions with two low-velocity basin structures.

Initial stresses

In our simulation, we adopted a triaxial principal stress scheme with two principal horizontal stresses, that is, σ_1 and σ_3 , and one vertical principal stress σ_2 . The stress ratio of these three principal stresses $R = 0.46$, as defined by $R = (\sigma_2 - \sigma_3) / (\sigma_1 - \sigma_3)$, is given by Xie *et al.* (1994) and Cui *et al.* (2006). The effective stress fields are described as follows:

$$\sigma_2 = 0.35\rho gh, \quad (1)$$

$$\sigma_1 = 1.38\sigma_2, \quad (2)$$

$$\sigma_3 = 0.68\sigma_2, \quad (3)$$

in which ρ is the rock density, g is the gravitational acceleration, and h is the depth. Two considerations should be mentioned here. The first is that the parameter h starts from the surface, not from sea level. The second is that we set σ_2 to increase from the surface to 5 km below the free surface

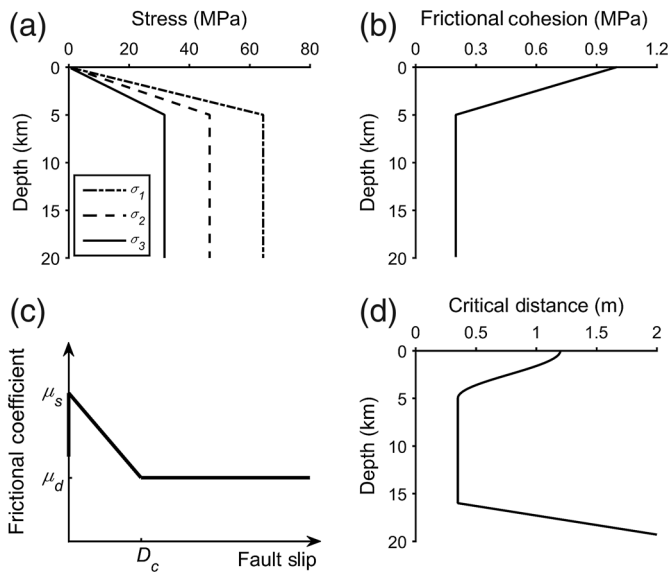


Figure 5. Schematics illustration of the (a) effective stress fields (σ), (b) frictional cohesion (C_0), (c) slip-weakening law, and (d) critical distance (D_c).

and then remain constant to avoid a large stress drop at the lower extent of the fault plane. Figure 5a provides an example of the distributions of the effective initial stresses with the depth.

As indicated in the Introduction, our research area is located at the southeastern tip of the Sichuan–Yunnan block, which moves toward the SE, causing the maximum horizontal compressive stress to act on the QF. A focal mechanism study revealed a relatively variable maximum principal stress azimuth in this area. Kan *et al.* (1977) and Zhang and Liu (1982) used *P*-wave first motions to obtain the focal mechanism of the Tonghai earthquake and showed that the maximum compressive principal stress orientation is N9°W and N12°W, respectively. The aftershock focal mechanisms of the Tonghai event illustrate different maximum principal stress directions ranging from N32°W to N41°W (Liu *et al.*, 1999). Liu *et al.* (1999) investigated the focal mechanisms of 50 local earthquakes with magnitudes greater than five spanning the period from 1950 to 1996, and they obtained an average regional maximum principal stress direction of N22°W. Cui *et al.* (2006) used the same method and obtained an average stress azimuth of N17°W. Here, we simulate six dynamic rupture models with maximum principal stress orientations varying from N10°W to N35°W at a 5° interval to find the optimal stress azimuth for the Tonghai earthquake. All of these models share the same parameters, including the vertical-dipping fault geometry, stress ratio, and friction coefficients. Therefore, any change in the stress orientation results in changes in the normal stress τ_n , shear stress τ_s , stress drop, etc. Moreover, we construct one stress rotation stress model on the previously defined complex dipping fault plane, which will be discussed in the Unbroken northwestern segment of the QF section.

In this case, the regional stress orientation rotates through an angle of 25°, that is, the maximum principal stress orientation in the southeastern segment of the QF is N25°W, whereas the maximum principal stress is orientated to the south (N0°W) in the west of Eshan (the northwestern QF segment).

Fracture criterion and nucleation zone

The slip-weakening law proposed by Ida (1972) and Andrews (1976), which is widely used in dynamic rupture simulations (Aochi and Fukuyama, 2002; Ma *et al.*, 2008; Douilly *et al.*, 2015), is adopted in the CG-FDM because of its efficiency, simplicity, and ease of application. Static and dynamic friction coefficients of $\mu_s = 0.45$ and $\mu_d = 0.24$, respectively, are applied on the whole fault plane (Fig. 5c). Once the shear stress τ_s on the fault plane exceeds the fault strength, $\mu_s \cdot \tau_n$, the rupture will propagate and release strain energy. Similar to the variations in the regional stresses with the depth, the slip-weakening distance D_c is 1.2 m at the free surface and decreases to 0.35 m from the surface to 5 km below the surface to consider the brittle layer of the crust. Then, D_c remains constant between 5 and 16 km and subsequently increases rapidly in the ductile layer (Scholz, 1988; Aochi and Fukuyama, 2002; Zhang *et al.*, 2017). The cohesive force C_0 is set to 1.0 MPa at the surface and decreases linearly to 0.2 MPa at a depth of 5 km, beyond which it has a constant value of 0.2 MPa (Fig. 5b,d). Moreover, there is one particular case that should be mentioned here; we set the cohesive force west of Eshan equal to 4 MPa in the C_0 increasing scenario, and it will be presented in the Unbroken northwestern segment of the QF section.

The nucleation point was set close to the hypocenter with a depth below the free surface of 13 km in our model (Zhang and Liu, 1978). In addition, we adopted three other nucleation positions, namely, Eshan, Wujie, and Quxi, in the Future potential earthquake scenarios section. We tested these three nucleation points on both the vertical-dipping fault geometry and the complex dipping fault geometry. The nucleation patch with a radius of 2.0 km was given a shear stress slightly larger (0.5%) than the fault strength to initialize the dynamic rupture. After the rupture initiates, it will propagate outside of the nucleation patch and cause spontaneous rupture according to its stress condition and the rupture criterion. Figure 6 presents an example of the normal stress τ_n , the shear stress τ_s , and the stress drop on a vertical fault plane with a maximum principal stress orientation of N25°W. The shear stress τ_s is similar to the result from Chen *et al.* (1982), which is 16.4 MPa, as estimated from the magnitudes of minor earthquakes, and the stress drop is also comparable to the result in Wang *et al.* (1978), which is 3.4 MPa.

As indicated in the Fault geometry model section, the ground surface topography is considered in our fault model; hence, in the following dynamic rupture and seismic-wave propagation simulations, the SRTM 90 m topography database (Jarvis *et al.*, 2008) was adopted in our computational domain.

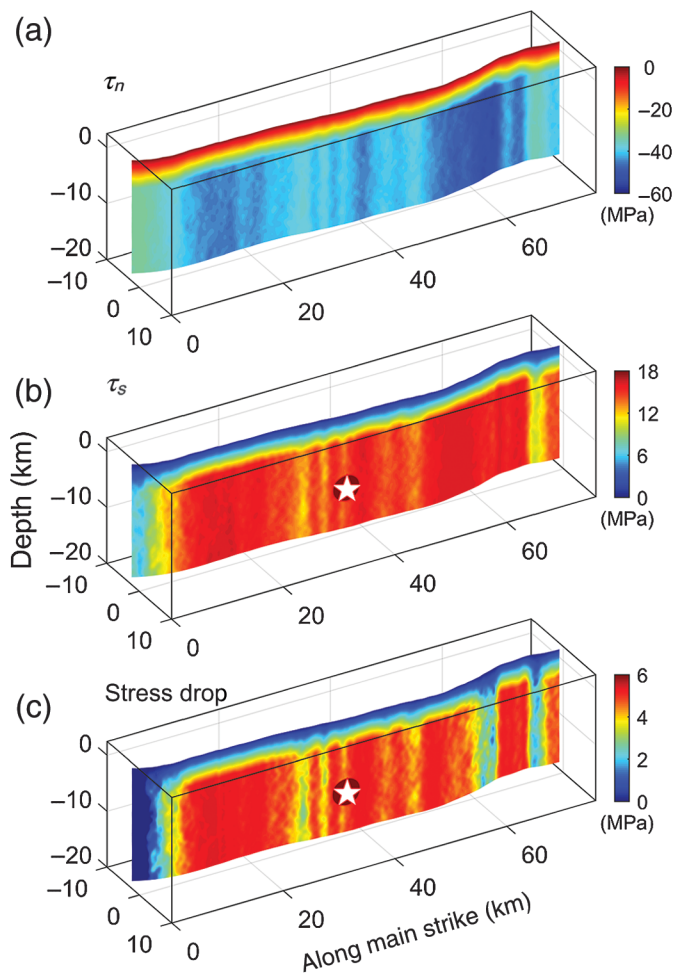


Figure 6. Example of the (a) normal stress τ_n , (b) shear stress τ_s , and (c) stress-drop distribution on the vertical-dipping fault plane. The maximum principal stress direction in this example is N25°W. The white star with the red edges denotes the nucleation point.

Our dynamic rupture simulation had the computational dimensions of 84, 10, and 24 km along the fault strike, normal, and dip directions, respectively, and the computational domain was discretized into $1680 \times 200 \times 480$ grids with a grid interval of 50 m. Technically, we can compute the wave propagation along with the rupture propagation. However, the computational domain of the wave propagation simulation is much larger (with dimensions of 182, 134, and 40 km in the longitudinal, latitudinal, and depth directions, respectively) than the area of the dynamic rupture simulation and will thus be extraordinarily time- and computational resources-consuming. Therefore, after we performed the dynamic rupture simulation, we put the dynamic source into the larger computational area to perform the wave propagation simulation. Here, we adopted a coarser grid with a grid interval of 200 m, and the computational area was discretized into $1080 \times 720 \times 200$ grids. It also should be mentioned here that the absorbing boundary condition was used not only in the dynamic rupture simulations

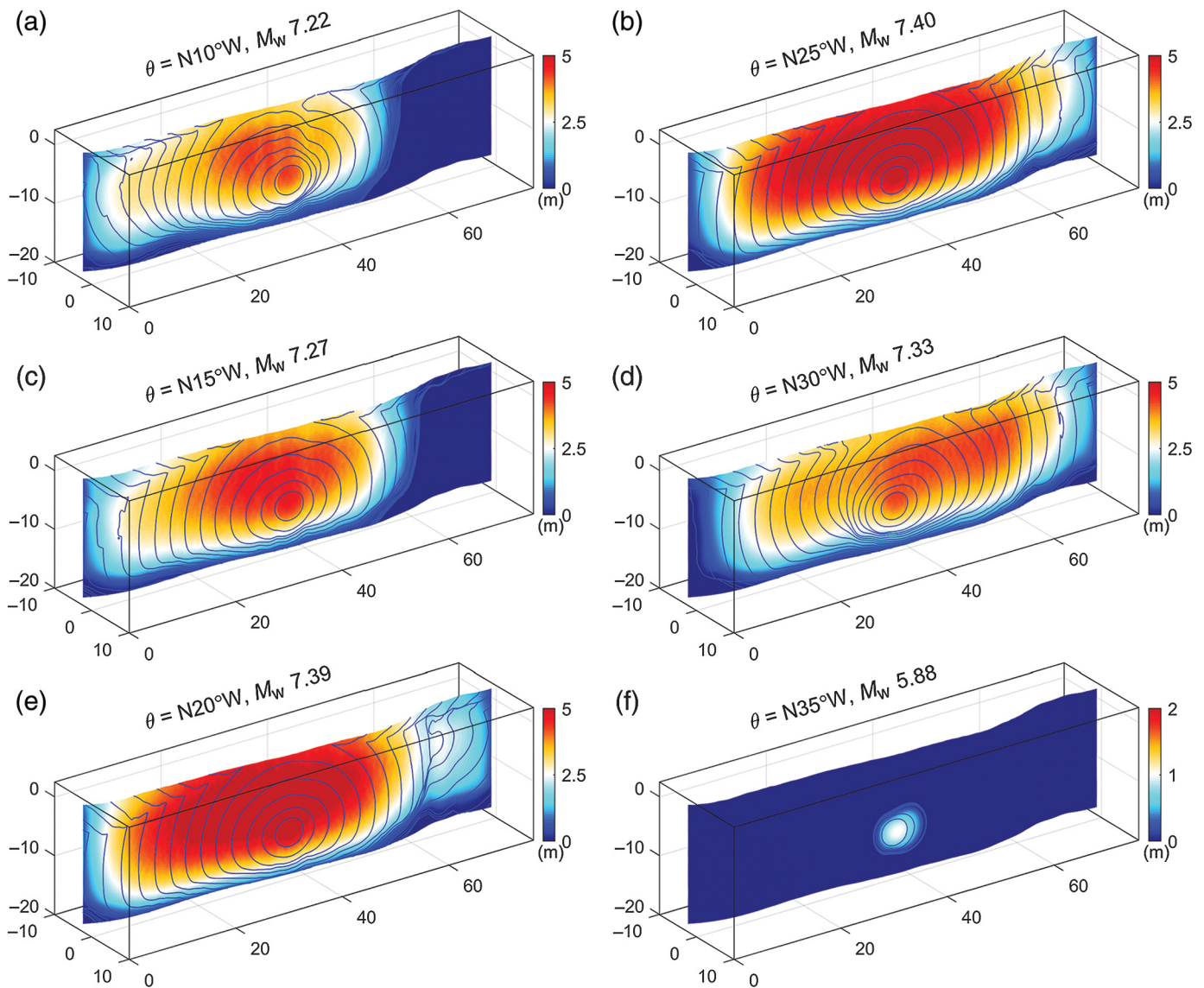
but also in the wave propagation simulations. Moreover, the time interval for both of these simulation steps was 0.004 s. The time duration for most of the dynamic rupture simulations was 24 s, and for most of the wave propagation simulations, it was 60 s. For the special future potential earthquake scenario case in which we used a vertical-dipping fault geometry and nucleation at Quxi, the time durations of the dynamic rupture and wave propagation simulations were 36 and 90 s, respectively.

RESULTS

Regional principal stress orientations

Figure 7 shows the distribution of the final slip and the rupture time contours from the dynamic rupture simulation of the QF plane with different stress orientations. When the stress azimuth is N10°W and N15°W, (Fig. 7a,c), the rupture successfully propagates to the northwestern segment of the QF after its initiation. However, when the rupture propagates 20 km to the southeastern part of the QF, the rupture front encounters the bending fault segment of the QF, and this fault segment with a change in its strike of nearly 30° acts as a strong barrier and stops the rupture from propagating further (Kase and Day, 2006). The difference between Figure 7a,c is that a slightly larger slip and moment magnitude are obtained when we set the stress azimuth θ equal to N15°W compared with setting θ to N10°W. Figure 7e,b,c demonstrates that when we set the maximum principal stress orientation to N20°W, N25°W, and N30°W, respectively, the rupture can propagate through the entire fault plane, but the rupture patterns and slip distributions differ. We further observe that when the rupture in Figure 7e propagates to the bending segment, it takes a few seconds for the rupture to accumulate sufficient energy to propagate through it. In contrast, in the cases of Figure 7b,d, the rupture propagates smoothly through the bending segment of the QF. Between the cases in Figure 7b,c, Figure 7b clearly has a larger moment magnitude. This means that when the maximum principal stress azimuth is N25°W, the dynamic rupture process produces a larger stress drop. In the aforementioned five simulations, most of the fault plane presents a sub-shear rupture mode. However, in the northwestern segments of Figure 7a,c and in the southeastern segments of Figure 7b,d, a supershear rupture can be observed, wherein the rupture velocity is greater than the V_S on the fault plane. When we set the stress azimuth θ equal to N35°W, the simulation reveals a different rupture pattern (Fig. 7f). The rupture propagates outside the nucleation patch for a few seconds and stops spontaneously, and the simulation gives a moment magnitude of 5.88; thus, this scenario should be identified as a self-arresting rupture, as defined by Xu *et al.* (2015). The fault-slip evolutions over time of these simulations can be found in the supplemental material (Videos S1–S6).

The horizontal peak ground velocity (PGVh) components calculated from the wave propagation simulations using previous

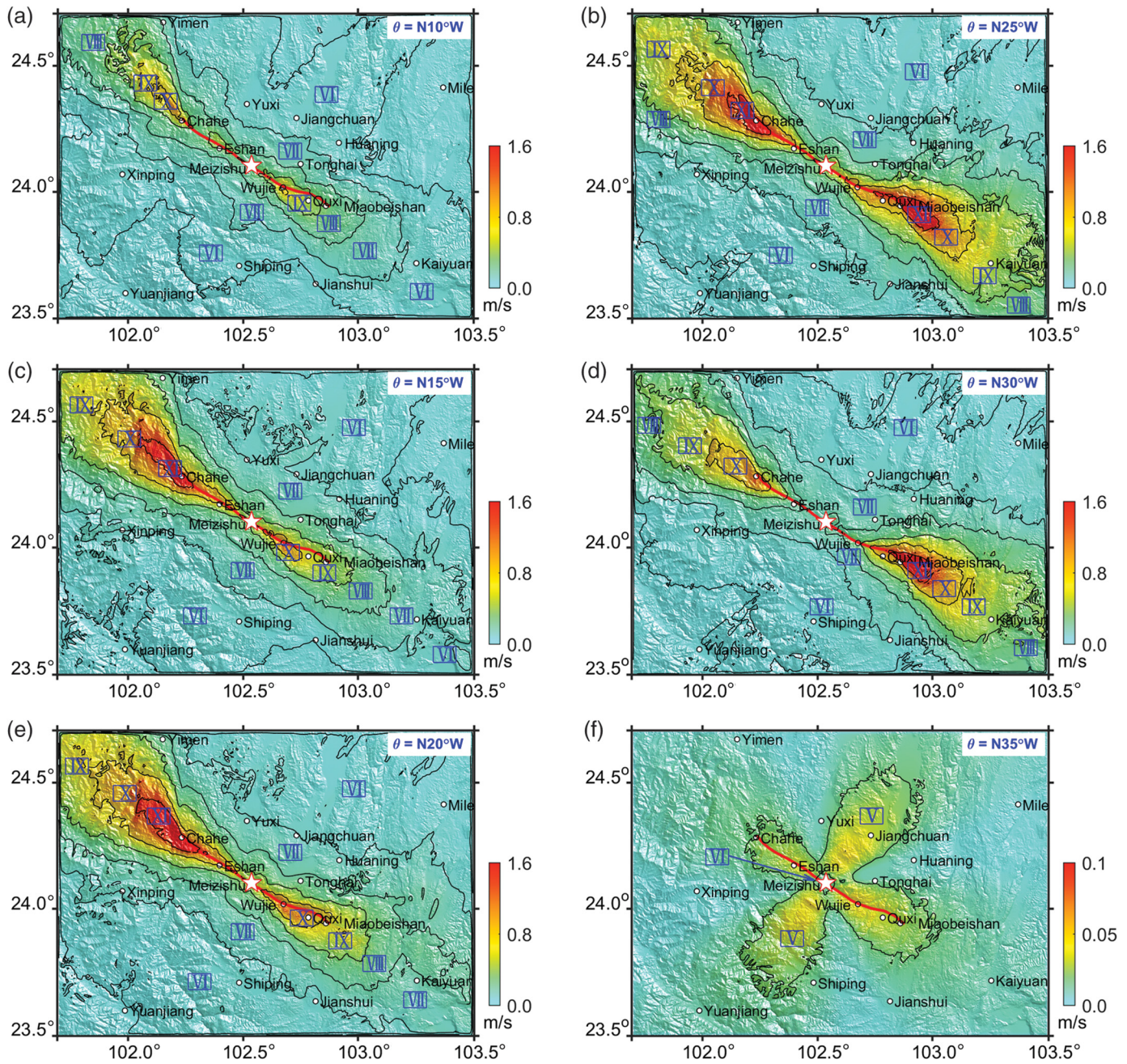


dynamic sources are presented in Figure 8, in which the black contour lines are the PGVh values applied based on the Chinese seismic intensity scale (Table 1). We find that the ground-motion distribution depends strongly on the stress orientations and each hazard distribution shows a unique strong ground motion pattern. When the stress azimuth ranges from N10°W to N30°W (Fig. 8a–e), all of the hazard distributions show a bilateral rupture damage pattern, and the maximum intensity is XI in Figure 8b–e. For the ground motion originating from the self-arresting rupture (Fig. 8f), that is, when the stress azimuth is N35°W, the seismic radiation pattern looks like a cross generated by a point source, and the maximum intensity close to the hypocenter is VI. In addition, the ground-motion patterns in Figure 8a,c,e are concentrated mainly in the northwestern part of the research area, whereas Figure 8b shows a damage distribution that is somewhat symmetrical about the epicenter and the damage in Figure 8d is distributed mainly in the southeastern part of the research area.

Figure 7. Final slip distribution and rupture time contours every 1 s on the fault plane from different principal stress orientations. The moment magnitudes are also plotted at the top of each subfigure. Panels (a–e) share the same colorbar scale, whereas (f) uses a different colorbar scale.

Moreover, the damage distributions in the southeastern part of the research area in Figure 8b,d are comparable to the documented intensity distribution.

According to the aftershock distributions reported by Zhang and Liu (1978) and Liu *et al.* (1999), we know that very few aftershocks were sourced from in the middle part of the QF, indicating that the middle part of the QF released more strain energy during the Tonghai earthquake. They also showed that the location of the maximum surface dislocation was very close to the epicenter. In Figure 7b, we show that our model slip distribution is concentrated near the epicenter. This model can optimally explain the deficiency of aftershocks

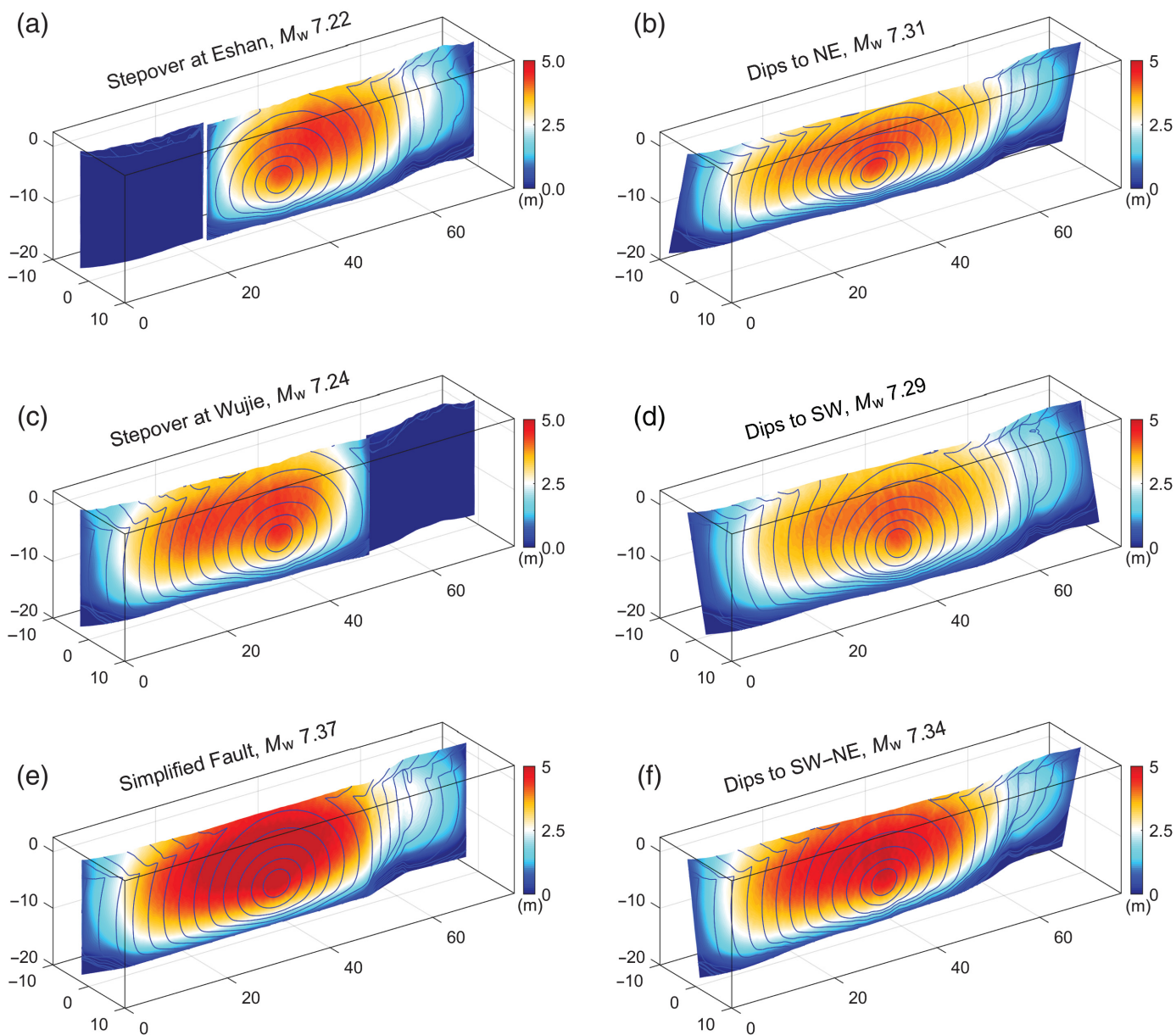


in the middle part of the QF and the location of the maximum surface dislocation. Therefore, we deduce that the maximum principal stress orientation of the Tonghai earthquake was roughly N25°W. Our dynamic rupture simulation result illustrates a rupture throughout the QF (Fig. 7b), and the intensity distribution in the southeastern part of the research area well matches the documented intensity distribution (Fig. 8b). However, the surface rupture observed during the field investigation suggests that the northwestern segment of the QF was unbroken during this earthquake, indicating that the fault rupture length in our simulation results is not consistent with the observations. Hence, some special conditions must have controlled the northwestern segment to allow it to remain unbroken during the Tonghai event, and we will discuss this phenomenon later.

Figure 8. Maps of the intensity distributions calculated from the horizontal peak ground velocity (PGVh) applied based on the Chinese seismic intensity scale. The PGVh values in (a–f) are simulated with the corresponding dynamic sources in Figure 7. The value of PGVh is represented by the color. The intensity scales are plotted as black contours with blue Roman numerals in blue boxes. The white star with red edges signifies the surface projection of the hypocenter, and the red line denotes the QF surface trace. The blue arrow in (f) points to the area with an intensity of VI. (a–e) share the same colorbar scale, whereas (f) uses a smaller colorbar scale.

Effects of the fault geometry

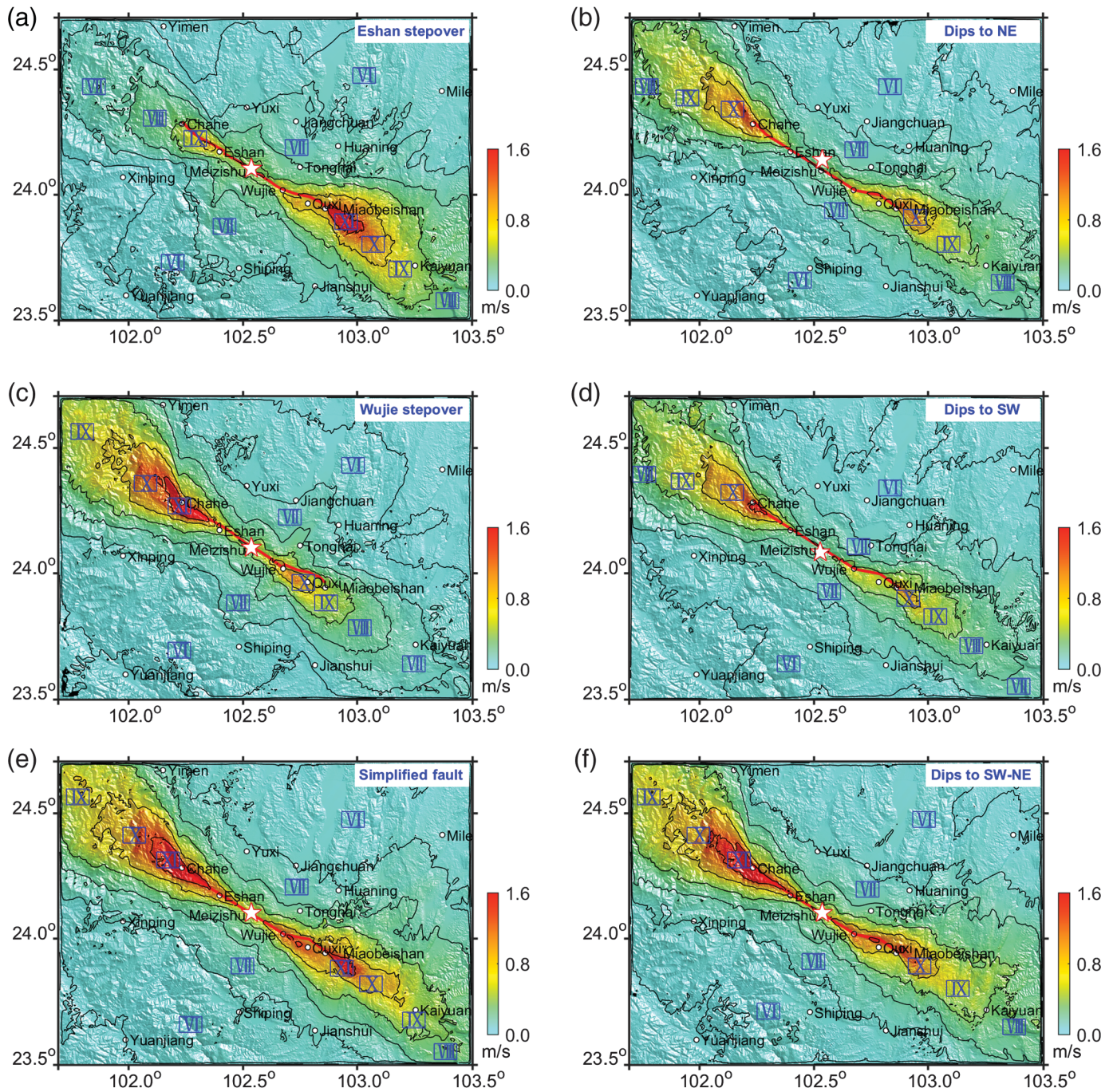
Figure 9a,c,e presents the dynamic rupture processes from the three fault models with different surface geometries. The fault geometry model with a stepover at Eshan (Fig. 9a) reveals a



primary fault presenting a rupture pattern and slip distribution along the southeastern part of the QF that is similar to the results shown in Figure 7b, whereas the secondary fault shows a different rupture pattern. The rupture propagates from the primary fault to the secondary fault at shallow depths, causing minor fault slipping and thus minor fault surface dislocations. However, the rupture cannot propagate to the deep part of the secondary fault plane, which may explain why there was no observed surface rupture in the northwestern part of the QF during the Tonghai earthquake. When the stepover is located at Wujie (Fig. 9c), the rupture pattern on the primary fault west of the epicenter is highly similar to the results of the counterpart in Figure 7b. However, the rupture on the secondary fault dies out quickly at shallow depths due to the fault strength. The results from this geometry model are not consistent with the Tonghai event because the surface rupture along the

Figure 9. Final slip distribution and rupture time contours every 1 s from the different fault geometry models. (a,c,e) Results from different fault surface traces, as indicated in Figure 3, whereas (b,d,f) results from different dipping fault models. (a,c,e) The fault surface trace features, (b,d,f) fault dip directions, and moment magnitudes are also plotted in the top of each subfigure. NE, northeast; SW, southwest; SW-NE, the QF dips toward the SW west of Eshan and dips toward the NE east of Eshan.

southeastern segment of the QF was well documented. For the result of the simplified fault model (Fig. 9e), the rupture propagates through the entire fault plane. The rupture pattern of the western part of the third fault segment is quite similar to the results from Figure 7b, albeit with a slightly smaller slip amplitude. The third fault segment shows a minor difference in the rupture speed compared with the counterpart in Figure 7b. In general, the simplified fault geometry model



reproduces the rupture pattern of the complex fault geometry model well.

Figure 9b,d,f presents the results of the dynamic rupture simulations from the previously defined dipping fault models. Figure 9b shows the distribution of the slip and the rupture pattern on a 75° NE-dipping fault, whereas Figure 9d shows the same for a 75° SW-dipping fault. Both ruptures propagate through the whole fault plane and present similar slip distributions and rupture time contours. Compared with the results of the vertical-dipping fault model in Figure 7b, these two dipping cases share a smaller slip amount and moment magnitude but a longer rupture time. The dynamic rupture simulation

Figure 10. Synthetic intensity distributions calculated from the PGVh component applied based on the Chinese seismic intensity scale. The PGVh values in (a–f) are simulated with the corresponding dynamic sources in Figure 9. The PGVh value is represented by the color. The intensity scales are plotted as blue contours with black Roman numerals in blue boxes. The white star with red edges signifies the surface projection of the hypocenter, and the red line denotes the QF surface trace. The meanings of NE, SW, and SW–NE are the same as in Figure 9.

result on the complex dipping fault geometry is presented in Figure 9f. Once we set the QF dipping toward the SW at the northwestern end with an 80° dipping angle and dipping

toward the NE at the southeastern end with a 75° dipping angle (SW–NE), the rupture propagates smoothly to the northwestern segment of the QF, but the rupture decelerates once it arrives at the bending segment. In comparison with the vertical-dipping fault model (Fig. 7b), we find that the main differences between the dynamic rupture simulation results from the vertical-dipping fault geometry and the complex dipping fault geometry are the rupture pattern and slip distribution on the eastern end of the QF in which the rupture speed is relatively low and the slip is small.

Figure 10 shows the distributions of the PGVh component in the aforementioned dynamic rupture models. The black contour lines are the seismic intensities calculated by the PGVh applied based on the Chinese seismic intensity scale (Table 1). These intensity maps show that the seismic hazard distribution is strongly dependent on the fault geometry, and all of the maps present a maximum intensity of XI, except Figure 10b,d, which have a maximum intensity of X. The results in the left column present the seismic intensity distributions of the fault models with different fault surface traces. As almost no rupture is observed on the secondary fault west of Eshan, the damage is concentrated mainly in the southeastern part of the research area (Fig. 10a), and the intensity appears to be the same as the counterpart in Figure 8b. Similarly, when the stepover is located at Wujie, the seismic damage is distributed mainly in the northwestern part of the research area. It is worth noting that the maximum intensity east of the stepover is X, even when there is almost no surface rupture on the secondary fault. The results in Figure 10e show the distribution of the PGVh component from the simplified fault geometry model. We find that the areas with intensities of IX and X are slimmer than the corresponding areas in Figure 8b; otherwise, the PGVh distributions are similar. The results of this intensity map and dynamic rupture simulation validate the use of a simplified fault model as a substitute for a complex curved, nonplanar QF geometry model.

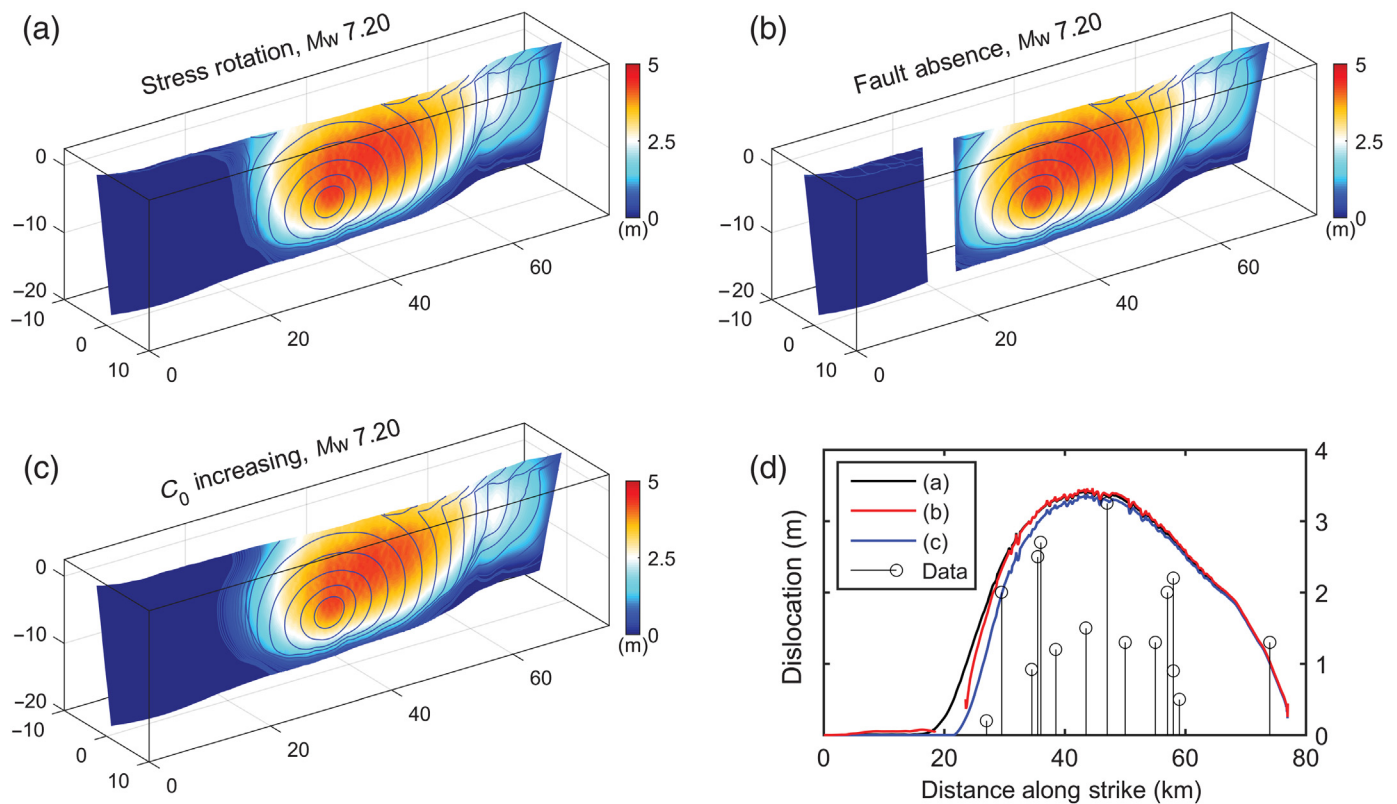
The PGVh maps in the right column show the ground-motion results from the three dipping fault models. When the QF dips toward the NE and SW, the seismic intensity distributions are similar (Fig. 10b,d). Severe damage is distributed mainly at the two ends of the QF, and the area with an intensity of X is smaller than the documented area at the southeastern part of the research area (Fig. 2). In addition, the dipping fault effect can be observed in these two cases in which large ground motions are concentrated on the hanging wall of the fault (Oglesby *et al.*, 2000; Duan, 2010; Rodgers *et al.*, 2019). If we use the dynamic source derived from a complex dipping fault model, a smaller PGVh distribution is observed in the southeastern part of the research area compared with that in Figure 8b because the maximum intensity is X in this region. This is in good agreement with the documented intensity distribution.

From the previous dynamic rupture and strong ground motion simulation results, we find that the fault geometry

model with a stepover at Eshan can explain the segment of the QF that remained unbroken during the Tonghai event with regard to the rupture length. However, the intensity distribution is not consistent because the high-intensity area is larger than the observed intensity distribution. In addition, the results from the fault model with a stepover at Wujie are not consistent with the data here. As mentioned before, well-observed surface ruptures and dislocations were reported to the east of Wujie (Zhang and Liu, 1978). The validation of the simplified fault geometry model suggests that a four-segment QF model can represent the complex nonplanar QF geometry well. Furthermore, an entirely NE-dipping and SW-dipping geometry may not be proper for the simulation of the Tonghai earthquake because the area with an intensity of X is smaller than the documented distribution of this intensity in the corresponding region. Therefore, we deduce that the QF probably dips toward the SW along its northwestern segment and toward the NE along its southeastern segment.

Unbroken northwestern segment of the QF

With the previously defined model settings, three scenarios that were used to explain the unbroken northwestern segment of the QF were modeled—stress rotation, C_0 increasing, and fault absence. The dynamic rupture simulation results are presented in Figure 11. The simulation results show a nearly unilateral rupture in each of these three numerical cases. Moreover, they exhibit similar rupture propagation characteristics to the east of the epicenter (Fig. 11a–c) because they have identical stress conditions, fault geometries, and friction parameters in the southeastern part of the QF. These three simulations show a slip asperity near the epicenter, and all give a moment magnitude of 7.2, which is the same as presented in figure 1 of Yan *et al.* (2018). However, the rupture to the west of the epicenter is different. If we establish the stress scheme with a regional stress rotation at Eshan, the rupture propagates approximately 15 km to the west along the strike, and the rupture gradually terminates near the free surface (Fig. 11a). Figure 1c demonstrates that when the cohesive force is increased along the northwestern segment, the rupture lasts approximately 10 s and then dies out slowly to the west of the epicenter of the middle segment of the QF. When we use a fault geometry model with a 5 km fault gap (the fault absence case in Fig. 11) for the simulation, the rupture clearly stops immediately at the western end of the main fault plane a few seconds later (Fig. 11b). Furthermore, the rupture is transferred to the northwestern QF plane, but the rupture becomes arrested quickly due to the fault strength, and the slip on the fault plane is negligible. Figure 11d presents the along-strike fault surface dislocations from these three numerical simulations and field geological observations (Zhang and Liu, 1978). The results show that the dislocations in these three cases are almost the same along the southeastern QF segment, and the surface slip from the stress rotation (black line) is slightly larger



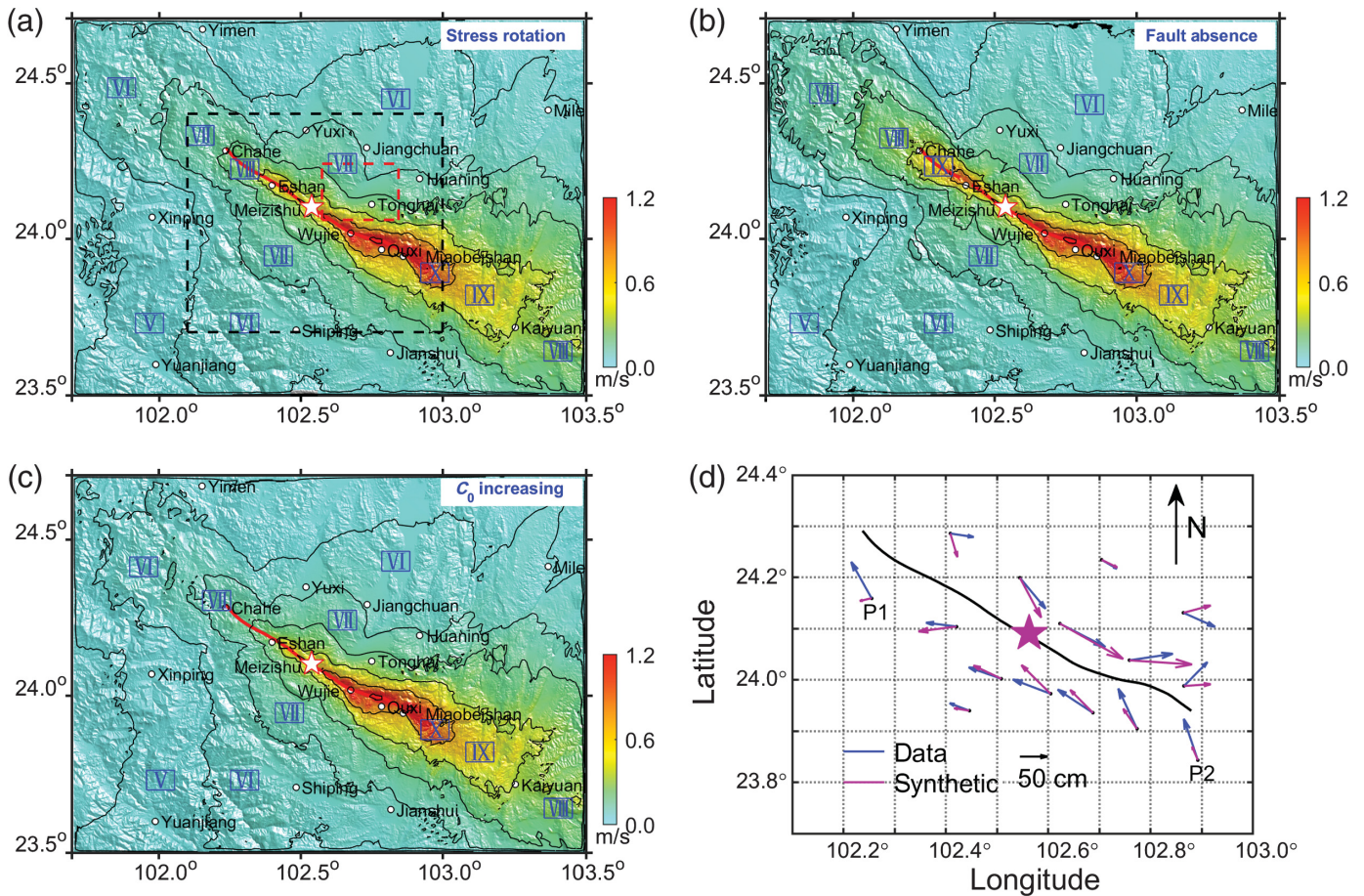
than the results from the cohesive force increase (blue line) and fault absence (red line) cases between 20 and 40 km along the QF. In general, all three cases are in good agreement with the documented fault dislocation data (matchsticks), especially the maximum fault surface slip and the values at both rupture ends.

Seismic-wave propagation modeling reveals that the PGVh maps exhibit very few differences because they have nearly identical dynamic sources (Fig. 12a–c). The PGVh intensity distribution applied based on the Chinese seismic intensity scale (Table 1) shares the main feature with the documented intensity (Fig. 2). The area with an intensity of X is consistent with the observed area. However, the zones with intensities of VIII and IX cover a large region in the southeastern part of the research area, whereas the zone with an intensity of VII covers less area on both sides of the epicenter. The former phenomenon may be caused by the strong rupture directivity and the absence of attenuation in our simulation program. In addition, the latter phenomenon can be explained by the fact that we did not incorporate sedimentary layers into our velocity model. Research from different authors showed that low-velocity sedimentary layers have significant impacts on ground motions, especially V_{S30} (Wills *et al.* 2000; Wald and Allen, 2007). However, for our simulation, we did not have detailed V_{S30} data. Second, if we possessed a V_{S30} velocity model, the simulations would need a much finer grid, which would require extraordinary amounts of time and computational resources. In addition, as presented in Figure 2, there was an intensity

Figure 11. (a,b,c) Final slip distribution and rupture time contours every 1 s on the fault plane from different modeling parameters that were used to explain the unbroken northwestern QF segment. The moment magnitude is also plotted in the top of each subfigure. (d) The final fault surface dislocations from the simulations (colored curves) versus the documented data (matchsticks).

anomaly in the Tonghai basin, where an area with an intensity of IX is surrounded by an area with an intensity of VIII. However, in these simulations, no intensity anomaly in the Tonghai basin is observed (area outlined by the red dashed rectangle in Fig. 12a).

Figure 12d presents a comparison of the horizontal deformations predicted from the results of the stress rotation with the absolute surface displacement data resolved from leveling surveys (National Seismological Bureau–The Geodetic Survey Brigade for Earthquake Research, 1975). We find that the synthetic data are in good agreement with the documented data, especially for locations close to the epicenter, with regard to both the displacement direction and the absolute values. P1 and P2 are the two locations with the worst similarity with regard to the deformation direction and absolute value, but as indicated by the author, these two points have the maximum error for the leveling survey method; thus, they may not represent the real deformations. In addition, the mismatching between the synthetic and observed data may be due to the simplification of the fault geometry, stress states, or other factors.



The low-velocity basin effect

In the preceding sections, we simulated the dynamic rupture and wave propagation processes of the Tonghai earthquake and reproduced the fault surface dislocations and surface displacements well. Here, we present another seismic-wave propagation simulation. We use the result from the **Unbroken northwestern segment of the QF** section and adopt the first possible scenario, that is, the stress rotation case (Fig. 10a), as the source time function. The only difference between the following simulation (Fig. 11a) and Figure 12a is that we add two small basins to the velocity model. As defined in the **Velocity model** section, the velocity structures of the Tonghai basin and Quxi basin are derived from He *et al.* (2013) and Wang *et al.* (2014), respectively, and the sedimentary basins are constructed in layers (Fig. 4c,d), with a minimum V_S of 400 m/s at the top of the basin.

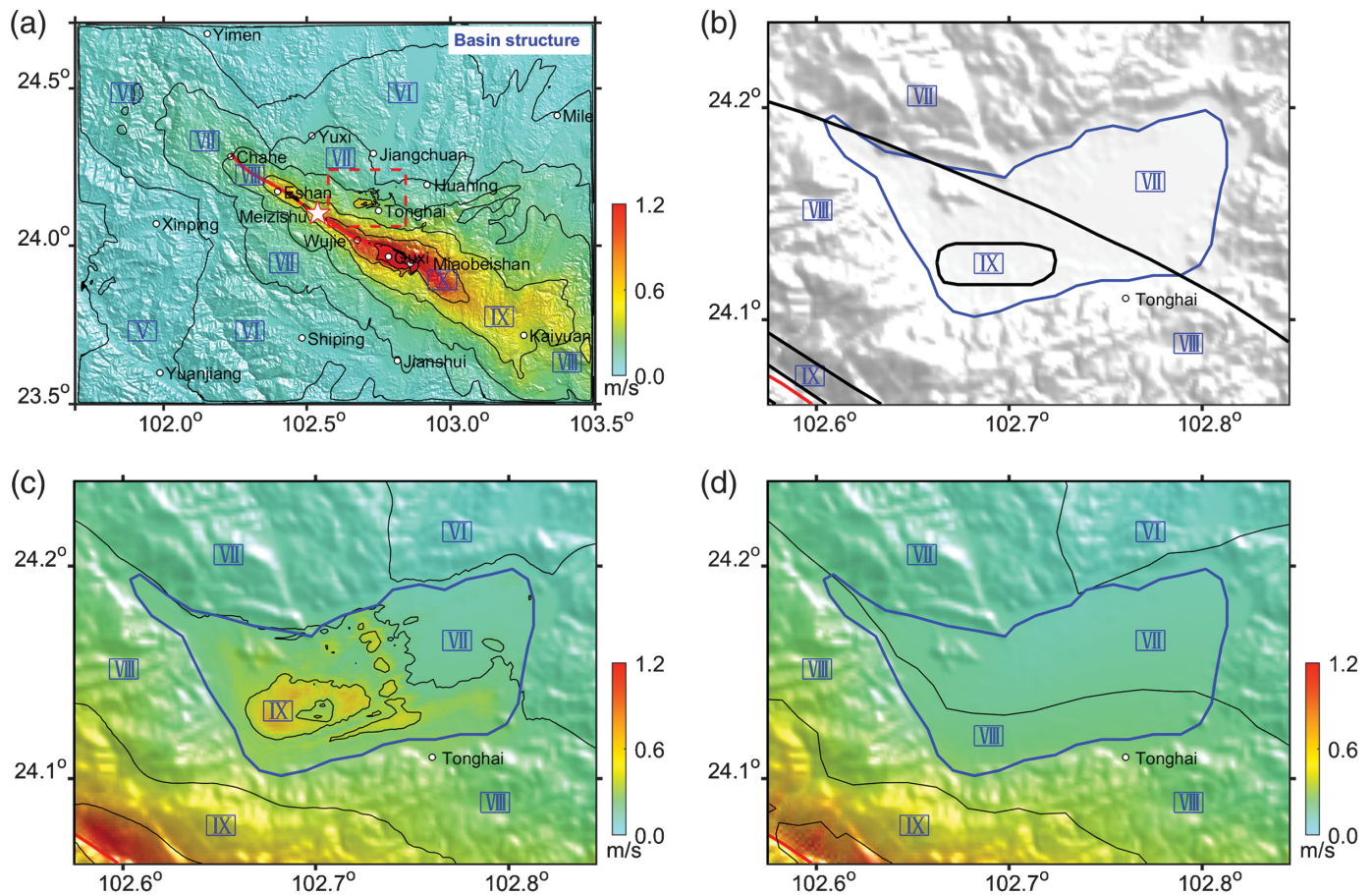
The simulation results are presented in Figure 13a. We find that the PGVh distribution is almost the same as the distribution shown in Figure 12a. At the same time, some differences can be found. First, the area with an intensity of IX is slightly larger than that in Figure 12a. Second, an intensity anomaly in the Tonghai basin is clearly observed (area emphasized by the red dashed rectangle), and this area is amplified in Figure 13c. Here, we also plot the documented intensity in the Tonghai area (Fig. 13b), as well as the corresponding part in Figure 12a

Figure 12. Maps of the synthetic intensity distributions calculated from the PGVh component. The PGVh values in (a–c) are simulated with the corresponding dynamic sources in Figure 11a–c. The red dashed rectangle emphasizes the location of the Tonghai basin. The black dashed rectangle illustrates the area in (d). (d) Comparison of the horizontal displacements predicted by the stress rotation model in (a) with the absolute surface deformation data resolved from leveling surveys. The long black line represents the QF surface trace, whereas the star denotes the epicenter. P1 and P2 are the two locations with the worst similarity with regard to the deformation direction and absolute value.

(Fig. 13d). This simulation reveals that the intensity anomaly in the Tonghai basin can be explained by a low-velocity basin structure.

Future potential earthquake scenarios

As an active boundary of the Sichuan–Yunnan block, the QF exhibits a right-lateral slip rate of 2.84–3.27 mm/yr, which was deduced from topographic displacements by Wang *et al.* (2014). Accordingly, we cannot expect the QF to remain tectonically quiet after the devastating Tonghai earthquake. Another damaging event will eventually occur tens, hundreds, or even thousands of years in the future. Hence, a serious problem for future seismic hazard assessments of the surrounding area is not whether an earthquake will come but where and

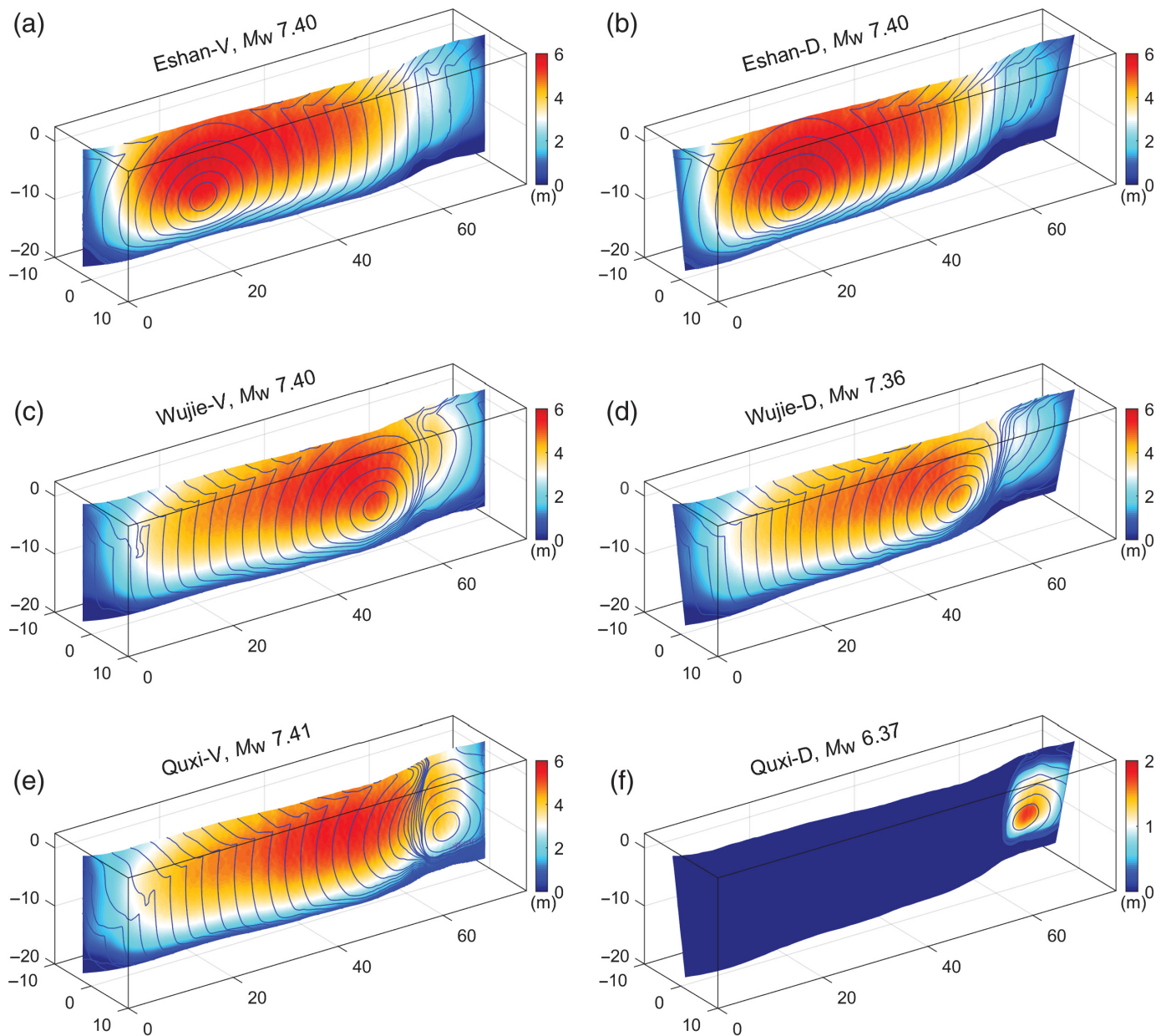


how damaging the next earthquake will be (Oglesby and Mai, 2012). We should therefore be prepared for the next destructive event as soon as possible. In this section, we simulate several potential earthquake scenarios using the previously identified fault geometry, velocity structure, and stress field, but the nucleation point is placed at various locations to investigate the possible future earthquake rupture dynamics and strong ground motions, which could help mitigate damage to the research area. For comparison, two fault geometries are adopted—one is the vertical-dipping fault model, and the other is the SW–NE-dipping fault model, which is hereafter known as the complex dipping fault model.

Figure 14 illustrates the final slip distribution and rupture time contours on the fault plane from the dynamic rupture simulations. The three nucleation simulation cases in Figure 14a,c,e are applied with the vertical-dipping fault geometry, whereas those in Figure 14b,d,f are applied with the complex dipping fault model. The nucleation point is located at Eshan due to its previous earthquake history—as mentioned before, the 1913 earthquake, which broke the northwestern segment of the QF, nucleated at Eshan. Our simulation results (Fig. 14a,b) present a rupture throughout the QF. Both models give a moment magnitude of 7.4. The maximum fault slip is close to 6 m for these two cases and occurs near the epicenter. The difference between Figure 14a,b is the slip distribution at the

Figure 13. (a) Maps of the PGVh distributions simulated from the dynamic sources of the stress rotation case in Figure 11a and the velocity model with two low-velocity zones in the Tonghai basin and Quxi basin. The PGVh value is represented by the color. The intensity scales are plotted as black contours with blue Roman numerals in blue boxes. The red line represents the QF surface trace, whereas the white star with red edges signifies the epicenter. The red dashed rectangle emphasizes the Tonghai area and is amplified in (c). (b) The documented intensity in the Tonghai area. (d) The intensity distribution in the Tonghai area from Figure 12a. Blue lines in (b,c) illustrate the margin of the Tonghai basin.

southeastern end of the QF. The fault slip in Figure 14b is slightly smaller than that in Figure 14a due to the fault geometry. We locate the nucleation point at Wujie because this location was once identified as the epicenter of the Tonghai earthquake (Han, 1980). The simulation results with nucleation at Wujie on the vertical fault and complex dipping fault models are presented in Figure 14c,d. We find that both ruptures propagate through the entire QF fault plane. However, the slip on the vertical fault plane is slightly larger than the slip on the complex dipping fault plane, leading to a slightly larger moment magnitude. The difference between Figure 14c and d is mainly concentrated in the bending fault segment of the QF. The bending fault segment does not substantially slow the rupture on the vertical-dipping fault model, whereas

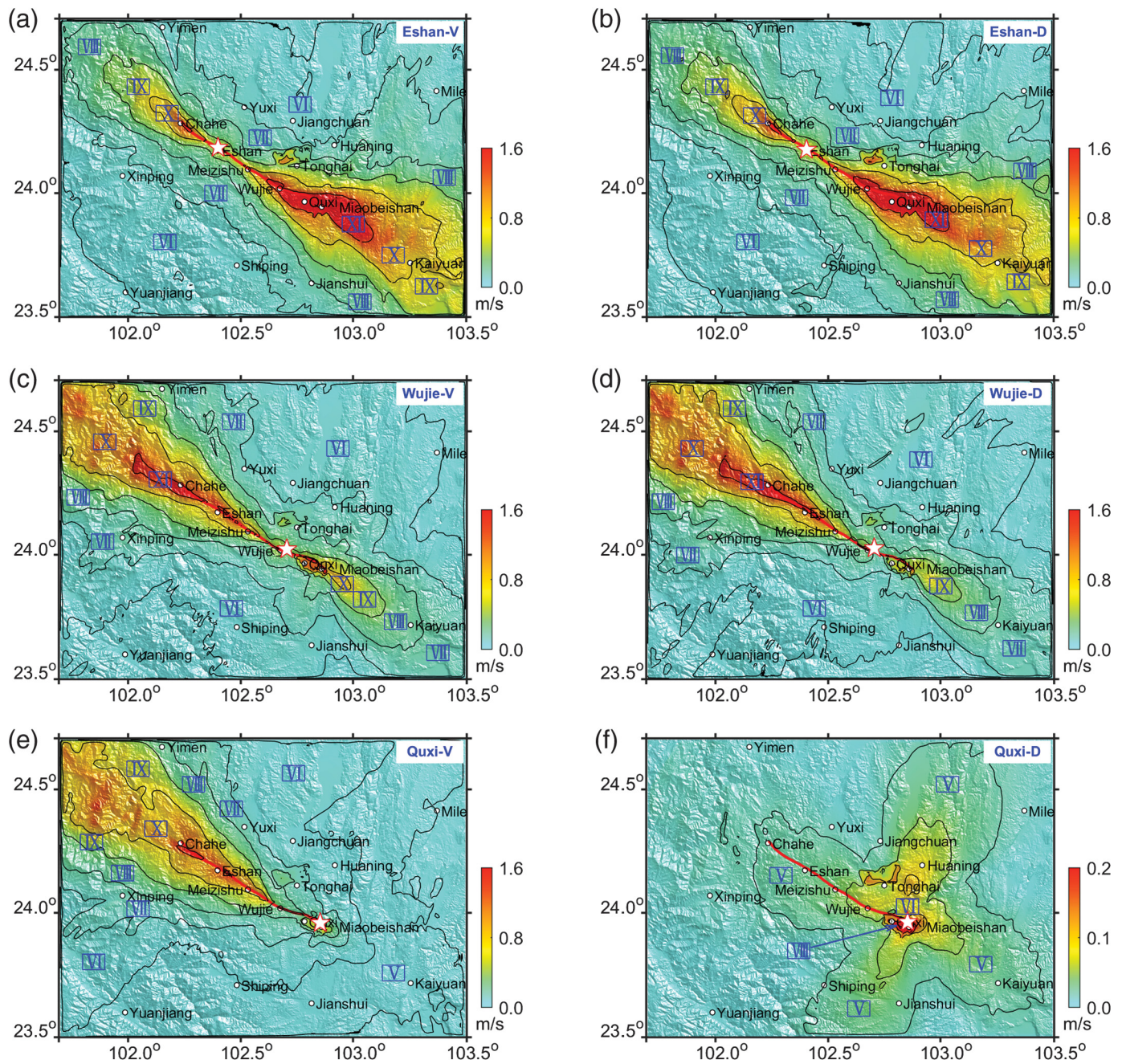


it stalls the rupture in Figure 14d for approximately 8 s. Then, the rupture speeds up again and propagates throughout the rest of the QF plane. Undoubtedly, the bending segment of the QF acts as a strong barrier and almost terminates the rupture. The rupture patterns are different when the nucleation point is placed at Quxi. Figure 14e illustrates that after the initiation of the rupture at the epicenter, the westward rupture velocity decreases dramatically, and the bending fault segment stalls the rupture for more than 10 s. Once the rupture transverse the bending segment, the rupture speeds up quickly and propagates over the rest of the fault plane at a nearly constant velocity. However, when we adopt the complex dipping fault model, the rupture propagates mainly up-dip and east in the strike direction and is confined to the southeastern end of the QF (Fig. 14f). The moment magnitude is much smaller in this

Figure 14. Final slip distributions and rupture time contours every 1 s on the QF plane from different nucleation points. (a,c,e) Results from the vertical dipping fault model, whereas (b,d,f) results from the complex dipping fault model. The nucleation locations and moment magnitudes are also plotted in the top of each subfigure. (a–e) share the same colorbar scale, whereas (f) uses a different colorbar scale. D, complex dipping fault geometry; V, vertical-dipping fault geometry.

case (M_w 6.37), whereas the corresponding scenario gives a moment magnitude of 7.41 (Fig. 14e).

The corresponding PGVh distributions are presented in Figure 15. The results are consistent with the confirmed conclusion that the damage pattern from an earthquake is controlled by the location of the epicenter (Oglesby and Mai, 2012; Aochi and Ulrich, 2015; Zhang *et al.*, 2017). Figure 15a–e



shows that the rupture directivity determines the intensity distribution. All five models present a maximum intensity of XI. When the epicenter is located at Eshan, the strong ground motion results from the vertical-dipping fault model in Figure 15a and the complex dipping fault model in Figure 15b are analogous to each other, and the rupture energy is distributed mainly within the southeastern region of the computational area. The second row in Figure 15 shows the PGVh distribution when the nucleation position is below Wujie. In the northwestern part of the epicenter, the intensity distribution in Figure 15c is similar to the results in Figure 15d. However, the intensity east of Quxi is different for these two cases because the maximum intensity is X in Figure 15c but IX in Figure 15d. Figure 15e,f shows the PGV results when the

Figure 15. Maps of future earthquake scenario intensity distributions calculated from the PGVh component according to the Chinese seismic intensity scale. The PGVh values in (a–f) are simulated with the corresponding dynamic sources in Figure 14. The PGVh value is represented by the color. The intensity scales are plotted as black contours with black Roman numerals in blue boxes. The red star signifies the surface projection of the hypocenter, and the red line denotes the QF surface trace. The blue arrow in (f) points to the area with an intensity of VIII. (a–e) share the same colorbar scale, whereas (f) uses a different colorbar scale. The meanings of V and D are the same as in Figure 14.

hypocenter is below Quxi. A severe damage potential can be observed in the northwestern region of the research area in Figure 15e, whereas the areas to the east and SE of the epicenter

are relatively safe. From the previous rupture simulation (Fig. 14f), we know that the dynamic rupture from the complex dipping fault model with nucleation at Quxi is constrained to the southeastern end of the QF, so the strong ground motion can affect only smaller areas (Fig. 15f). However, caution should be exercised regarding the area in the Quxi basin because it presents a maximum intensity of VIII due to the effects of the low-velocity basin structure. Another interesting phenomenon that can be found in Figure 15 in all six simulations is that an intensity anomaly exists in the Tonghai basin. Again, these results point to the importance of low-velocity sedimentary structures.

DISCUSSION

Effects of the surface topography

It was mentioned in the [Numerical Method and Model Construction](#) section that we constructed the fault geometry model with the topography and we simulated the dynamic rupture and wave propagation with the irregular topography in the computational area. Many works have shown that the topography could impact not only the rupture dynamics (Zhang *et al.*, 2016; Huang *et al.*, 2018) but also the strong ground motions (Zhang *et al.*, 2008; Lee *et al.*, 2009). Zhang *et al.* (2016) and Huang *et al.* (2018) have shown that the fault-plane topography can drive the rupture into a supershear rupture mode in some circumstances, consequently affecting the ground motion. The impact of the topography on the wave propagation has been discussed (Zhang *et al.*, 2008; Lee *et al.*, 2009; Zhu *et al.*, 2013, 2016). Their results emphasized that the topography contributes to generating high-frequency components. Ground motions, such as PGVh, will be amplified in the crest region and will be decreased in the valley region. In our work, first, the topographic relief exists, and the maximum elevation difference in the wave propagation simulation area can reach 2 km (Fig. 1), which leads us to incorporate the irregular topography into our simulations from a realistic perspective. Second, the topography effect is not the focus of our discussion. Therefore, we provide the dynamic rupture simulation and strong ground motion results with a flat topography model in the supplemental material. Third, the topography relief along the fault plane is relatively small (about a few hundred meters), and the final slip distribution and rupture pattern have minor differences relative to the case that has no surface topography (Fig. 7b and Fig. S1). However, the topography effect can still be clearly observed in the ground-motion results (Figs. S2 and S3).

CONCLUSIONS

We numerically simulated the spontaneous dynamic rupture and subsequent seismic-wave propagation processes of the 1970 Tonghai earthquake and several future potential earthquake scenarios along the QF, which is located at the southeastern tip of the Sichuan–Yunnan block, Yunnan, China. Using the same 3D

heterogeneous media and a vertical-dipping nonplanar fault geometry model, we first investigated the local maximum principal stress orientation. The simulation results suggest that the stress azimuth of the Tonghai event was most likely N25°W. Then, we tested three fault geometry models deduced from different fault surface traces, as well as three different dipping fault models. Our simulations show that the rupture on the primary fault could not have transferred to the secondary fault under our stress scheme for either stepover fault model. These results implied that the model with a stepover located at Wujie might not be convincing. Moreover, although there was almost no surface rupture west of the stepover when it was located at Eshan, the synthetic intensity distribution was not consistent with the documented intensity distribution. This stepover fault model may explain the unbroken northwestern segment of the QF under other fault geometry or stress conditions, such as a dipping fault geometry model with a stepover located at Eshan, which will be presented in future work. A simulation of a simplified four-segment geometry model of the QF validated the simplification of the complex curved QF model. This result emphasized that, if a detailed fault surface geometry model is not available, a multi-segment fault model that captures the main features of the fault strike can be an ideal substitution in performing numerical simulations. Numerical modeling of the dipping fault model indicated that the QF is not likely to dip entirely toward either the NE or the SW. Instead, a complex dipping fault model in which the QF dips toward the SW in its northwestern segment and toward the NE in its southeastern segment is preferred.

Subsequently, we provided explanations for the unbroken northwestern segment of the QF during the Tonghai earthquake. We did not provide definite causes for this phenomenon but presented possible scenarios. As a result, a rotation of the regional stress orientation caused by historical earthquakes, an increase in the cohesive force during the interseismic period, and a fault-absence geometry model each may explain the unbroken fault plane of the QF during the Tonghai event. Moreover, a small low-velocity basin was adopted in the velocity structure to explain the intensity anomaly in the Tonghai basin, and the results matched well. Finally, we performed simulations on the QF with two fault geometry models and three nucleation positions. The results showed a considerable hazard potential along the QF and nearby regions for both fault models when the nucleation point was placed at Eshan and Wujie. However, when we initiated the rupture at Quxi, an earthquake scenario with a vertical-dipping fault model could cause severe damage to most parts of the research area, whereas an earthquake scenario with a complex dipping fault model was constrained to the Quxi area. However, we should still take this case seriously because it produces a maximum intensity of VIII.

DATA AND RESOURCES

The fault surface traces are modified from Zhu (1984, 1985) and Wang *et al.* (2014). The Shuttle Radar Topography Mission (SRTM)

topography data are from [Jarvis et al. \(2008\)](#) and are available at <http://srtm.csi.cgiar.org> (last accessed December 2019). The low-velocity model in the two basins is modified from [He et al. \(2013\)](#), and the V_S velocity model is from [Shen et al. \(2016\)](#). The documented intensity, the fault surface dislocations, and the surface displacement data can be found in [Liu et al. \(1999\)](#). All figures were generated using MATLAB (<http://www.mathworks.com/products/matlab>, last accessed February 2020) and Generic Mapping Tools (<http://gmt.soest.hawaii.edu>, last accessed February 2020). The supplemental material contains three figures mentioned in the [Discussion](#) section (Figs. S1–S3) and six fault-slip evolution videos in the [Regional principal stress orientation](#) section, from Videos S1 to S6.

ACKNOWLEDGMENTS

The authors are grateful to Associate Editor Luis Angel Dalguer and two anonymous reviewers for their constructive comments. This work is supported by the National Natural Science Foundation of China (Grant Numbers 41790465 and 41922024), National Key R&D Program of China (2017YFC1500205), and Science and Technology Innovation Committee Foundation of Shenzhen (Grant Number KQTD20170810111725321). The simulations were performed in the National Supercomputing Center in Shenzhen (China).

REFERENCES

Aagaard, B. T., M. G. Knepley, and C. A. Williams (2013). A domain decomposition approach to implementing fault slip in finite-element models of quasi-static and dynamic crustal deformation, *J. Geophys. Res.* **118**, 3059–3079, doi: [10.1002/jgrb.50217](https://doi.org/10.1002/jgrb.50217).

Andrews, D. J. (1976). Rupture propagation with finite stress in anti-plane strain, *J. Geophys. Res.* **81**, 3575–3582.

Andrews, D. J., and M. Barall (2011). Specifying initial stress for dynamic heterogeneous earthquake source models, *Bull. Seismol. Soc. Am.* **101**, 2408–2417, doi: [10.1785/0120110012](https://doi.org/10.1785/0120110012).

Aochi, H., and E. Fukuyama (2002). Three-dimensional nonplanar simulation of the 1992 Landers earthquake, *J. Geophys. Res.* **107**, no. B2, 2035.

Aochi, H., and A. Kato (2010). Dynamic rupture of crosscutting faults: A possible rupture process for the 2007 M_w 6.6 Niigata-ken Chuetsu-Oki earthquake, *J. Geophys. Res.* **115**, no. B05310, 1–10, doi: [10.1029/2009JB006556](https://doi.org/10.1029/2009JB006556).

Aochi, H., and R. Madariaga (2003). The 1999 İzmit, Turkey, earthquake: Nonplanar fault structure, dynamic rupture process, and strong ground motion, *Bull. Seismol. Soc. Am.* **93**, 1249–1266, doi: [10.1785/0120020167](https://doi.org/10.1785/0120020167).

Aochi, H., and T. Ulrich (2015). A probable earthquake scenario near Istanbul determined from dynamic simulations, *Bull. Seismol. Soc. Am.* **105**, 1468–1475, doi: [10.1785/0120140283](https://doi.org/10.1785/0120140283).

Brocher, T. M. (2005). Empirical relations between elastic wavespeeds and density in the earth's crust, *Bull. Seismol. Soc. Am.* **95**, 2081–2092, doi: [10.1785/0120050077](https://doi.org/10.1785/0120050077).

Chaljub, E., E. Maufroy, P. Moczo, J. Kristek, F. Hollender, P. Brad, E. Priolo, P. Klin, F. Martin, Z. Zhang, et al. (2015). 3-D numerical simulations of earthquake ground motion in sedimentary basins: Testing accuracy through stringent models, *Geophys. J. Int.* **201**, 90–111, doi: [10.1093/gji/ggu472](https://doi.org/10.1093/gji/ggu472).

Chen, P., Z. Liu, R. Kan, and J. Qin (1982). An estimation of shear stress values of the surrounding regions before and after

the major Tonghai earthquake of 1970 from both the magnitudes ML and MS of minor earthquakes, *Acta Seismol. Sinica* **4**, no. 3, 227–238.

Chen, Y., H. Gu, and Z. Lu (1975). Variations of gravity before and after the Haicheng earthquake, 1975 and the Tangshan earthquake, 1976, *Acta Seismol. Sinica* **2**, 21–31.

Chen, Y., L. Huang, B. Lin, M. Liu, and X. Wang (1979). A dislocation model of the Tangshan earthquake of 1976 from the inversion of geodetic data, *Chin. J. Geophys.* **22**, 201–217.

Cui, X., F. Xie, and H. Zhang (2006). Recent tectonic stress field zoning in Sichuan-Yunnan region and its dynamic interest, *Acta Seismol. Sinica* **28**, 451–461.

Deng, Q., P. Zhang, Y. Ran, X. Yang, W. Min, and Q. Chu (2002). Basic characteristics of the active tectonics of China, *Sci. China Earth Sci.* **32**, 1020–1031.

Douilly, R., H. Aochi, E. Calais, and A. M. Freed (2015). Three-dimensional dynamic rupture simulations across interacting faults: The Mw 7.0, 2010, Haiti earthquake, *J. Geophys. Res.* **120**, 1108–1128.

Duan, B. (2008). Effect of low-velocity fault zones on dynamic ruptures with nonelastic off-fault response, *Geophys. Res. Lett.* **35**, L04307, doi: [10.1029/2008GL033171](https://doi.org/10.1029/2008GL033171).

Duan, B. (2010). Role of initial stress rotations in rupture dynamics and ground motion: A case study with implications for the Wenchuan earthquake, *J. Geophys. Res.* **115**, no. B05301, doi: [10.1029/2009JB006750](https://doi.org/10.1029/2009JB006750).

Duan, B., and D. D. Oglesby (2006). Heterogeneous fault stresses from previous earthquakes and the effect on dynamics of parallel strike-slip faults, *J. Geophys. Res.* **111**, no. B05309, doi: [10.1029/2005JB004138](https://doi.org/10.1029/2005JB004138).

Dunham, E. M., D. Belanger, L. Cong, and J. E. Kozdon (2011). Earthquake ruptures with strongly rate-weakening friction and off-fault plasticity, part 2: Nonplanar faults, *Bull. Seismol. Soc. Am.* **101**, no. 5, 2308–2322.

Duru, K., and E. M. Dunham (2016). Dynamic earthquake rupture simulations on nonplanar faults embedded in 3D geometrically complex, heterogeneous elastic solids, *J. Comput. Phys.* **305**, 185–207.

Ewald, M., H. Igel, K.-G. Hinzen, and F. Scherbaum (2006). Basin-related effects on ground motion for earthquake scenarios in the Lower Rhine Embayment, *Geophys. J. Int.* **166**, no. 1, 197–212.

Galvez, P., J. P. Ampuero, L. A. Dalguer, S. N. Somala, and T. F. Nissen-Meyer (2014). Dynamic earthquake rupture modelled with an unstructured 3-D spectral element method applied to the 2011 M 9 Tohoku earthquake, *Geophys. J. Int.* **198**, 1222–1240, doi: [10.1093/gji/ggu203](https://doi.org/10.1093/gji/ggu203).

Guo, S., Z. Li, S. Cheng, X. Chen, X. Chen, Z. Yang, and R. Li (1977). Discussion on the regional structural background and the seismogenic model of the Tangshan earthquake, *Sci. Geol. Sin.* **4**, 305–321.

Han, M. (1980). A discussion on the location of 1970 Tonghai earthquake of magnitude 7.7 in Yunnan province, *Seismol. Geol.* **2**, 30.

Harris, R. A., M. Barall, B. Aagaard, S. Ma, D. Roten, K. Olsen, B. Duan, D. Liu, B. Luo, K. Bai, et al. (2018). A suite of exercise for verifying dynamic earthquake rupture codes, *Seismol. Res. Lett.* **89**, 1146–1162.

He, Z., G. Hu, L. Lu, W. Zhang, T. Ye, and K. Shen (2013). The shallow velocity structure for the Tonghai basin in Yunnan, *Chin. J. Geophys.* **56**, 3819–3827.

- Hu, F., J. Wen, and X. Chen (2018). High frequency near-field ground motion excited by strike-slip step overs, *J. Geophys. Res.* **123**, doi: [10.1002/2017JB015027](https://doi.org/10.1002/2017JB015027).
- Huang, H., Z. Zhang, and X. Chen (2018). Investigation of topographical effects on rupture dynamics and resultant ground motions, *Geophys. J. Int.* **212**, 311–323, doi: [10.1093/gji/ggx425](https://doi.org/10.1093/gji/ggx425).
- Ida, Y. (1972). Cohesive force across the tip of a longitudinal-shear crack and Griffith's specific surface energy, *J. Geophys. Res.* **77**, 3796–3805.
- Jarvis, A., H. I. Reuter, A. Nelson, and E. Guevara (2008). *Hole-Filled SRTM for the Globe*, Version 4, available from the CGIAR-CSI SRTM 90m Database, available at <http://srtm.csi.cgiar.org> (last accessed October 2016).
- Kan, R., S. Zhang, F. Yan, and L. Yu (1977). Present tectonic stress field and its relation to the characteristics of recent tectonic activity in southwestern China, *Chin. J. Geophys.* **20**, 96–109.
- Kase, Y., and S. M. Day (2006). Spontaneous rupture processes on a bending fault, *Geophys. Res. Lett.* **33**, L10302, doi: [10.1029/2006GL025870](https://doi.org/10.1029/2006GL025870).
- Lee, S.-J., Y.-C. Chan, D. Komatitsch, B.-S. Huang, and J. Tromp (2009). Effects of realistic surface topography on seismic ground motion in the Yangminshan region of Taiwan based upon the spectral-element method and LiDAR DTM, *Bull. Seismol. Soc. Am.* **99**, no. 2A, 681–693, doi: [10.1785/0120080264](https://doi.org/10.1785/0120080264).
- Liu, X., J. Ma, X. Du, S. Zhu, L. Li, and D. Sun (2016). Recent movement changes of main fault zones in the Sichuan-Yunnan region and their relevance to seismic activity, *Sci. China Earth Sci.* **59**, 1267–1282.
- Liu, Z., F. Huang, and Z. Jin (1999). *The 1970 Tonghai Earthquake*, Seismological Press, Beijing, China.
- Ma, S., S. Custódio, R. J. Archuleta, and P. Liu (2008). Dynamic modeling of the 2004 Mw 6.0 Parkfield, California, earthquake, *J. Geophys. Res.* **113**, no. B02301, doi: [10.1029/2007JB005216](https://doi.org/10.1029/2007JB005216).
- Muhuri, S. K., T. A. Dewers, T. E. Scott Jr., and Z. Reches (2003). Interseismic fault strengthening and earthquake-slip instability: Friction or cohesion?, *Geology* **31**, 881–884.
- National Seismological Bureau–The Geodetic Survey Brigade for Earthquake Research (1975). The characteristics of the crustal deformation association with the Tonghai earthquake, Yunnan, in January 1970, *Chin. J. Geophys.* **18**, 240–245.
- Oglesby, D. D., and P. M. Mai (2012). Fault geometry, rupture dynamics and ground motion from potential earthquakes on the North Anatolian Fault under the Sea of Marmara, *Geophys. J. Int.* **188**, 1071–1087, doi: [10.1111/j.1365-246X.2011.05289.x](https://doi.org/10.1111/j.1365-246X.2011.05289.x).
- Oglesby, D. D., R. J. Archuleta, and S. B. Nielsen (2000). The three-dimensional dynamics of dipping faults, *Bull. Seismol. Soc. Am.* **90**, 616–628.
- Rodgers, A. J., A. Pitarka, and D. B. McCallen (2019). The effect of fault geometry and minimum shear wavespeed on 3D ground-motion simulations for an M_w 6.5 Hayward fault scenario earthquake, San Francisco Bay Area, Northern California, *Bull. Seismol. Soc. Am.* **109**, no. 4, 1265–1281, doi: [10.1785/0120180290](https://doi.org/10.1785/0120180290).
- Scholz, C. H. (1988). The brittle-plastic transition and the depth of seismic faulting, *Geol. Rundsch.* **77**, 319–328.
- Semblat, J. F., A. Kham, E. Parara, P. Y. Bard, K. Pitilakis, K. Makra, and D. Raptakis (2005). Seismic wave amplification: Basin geometry vs soil layering, *Soil Dynam. Earthq. Eng.* **25**, no. 7, 529–538, doi: [10.1016/j.soildyn.2004.11.003](https://doi.org/10.1016/j.soildyn.2004.11.003).
- Shen, W., M. H. Ritzwoller, D. Kang, Y. Kim, F.-C. Lin, J. Ning, W. Wang, Y. Zheng, and L. Zhou (2016). A seismic reference model for the crust and uppermost mantle beneath China from surface wave dispersion, *Geophys. J. Int.* **206**, 954–979, doi: [10.1093/gji/ggw175](https://doi.org/10.1093/gji/ggw175).
- Shi, Z., and S. M. Day (2013). Rupture dynamics and ground motion from 3-D rough-fault simulations, *J. Geophys. Res.* **118**, 1122–1141, doi: [10.1002/jgrb.50094](https://doi.org/10.1002/jgrb.50094).
- Sun, J., Y. Yuan, Z. Wen, X. Li, W. Du, J. Lin, S. Li, L. Zhang, A. Liu, F. Zhao, et al. (2008). *The Chinese Seismic Intensity Scale*, GB/T 17742-2008, <http://openstd.samr.gov.cn/bzgk/gb/newGbInfo?hcno=AE2DAA79A7404FFAC73A9F3A33FBAA5A> (last accessed February 2020).
- Tan, K., Q. Wang, J. Yu, Z. Nie, and C. Zhang (2017). Preliminary study result of the Coseismic deformation and rupture slip of the 1970 Tonghai earthquake, Yunnan province, *J. Geodes. Geodyn.* **37**, 331–354.
- Tapponnier, P., G. Peltzer, A. Y. Le Dain, R. Armijo, and P. Cobbold (1982). Propagation extrusion tectonics in Asia: New insights from simple experiments with plasticine, *Geology* **10**, 611–616.
- Tenthorey, E., and S. F. Cox (2006). Cohesive strengthening of fault zones during the interseismic period: An experimental study, *J. Geophys. Res.* **111**, no. B09202, doi: [10.1029/2005JB004122](https://doi.org/10.1029/2005JB004122).
- Wald, D. J., and T. I. Allen (2007). Topographic slope as a proxy for seismic site conditions and amplification, *Bull. Seismol. Soc. Am.* **97**, 1379–1395.
- Wang, C., C. Zhu, and Y. Liu (1978). Deformation of earthquake fault parameter for the Tonghai earthquake from ground deformation data, *Chin. J. Geophys.* **21**, 191–198.
- Wang, Y., B. Zhang, J. Hou, and X. Xu (2014). Structure and tectonic geomorphology of the Qujiang fault at the intersection of the Ailao Shan–Red River fault and the Xianshuihe–Xiaojiang fault system, China, *Tectonophysics* **634**, 156–170, doi: [10.1016/j.tecto.2014.07.031](https://doi.org/10.1016/j.tecto.2014.07.031).
- Wei, W., Z. Jiang, Y. Wu, X. Liu, J. Zhao, Q. Li, and M. Dong (2012). Study on motion characteristics and strain accumulation of Xiaojiang fault zone, *J. Geodes. Geodyn.* **32**, 11–15.
- Wen, X., F. Du, F. Long, J. Fan, and H. Zhu (2011). Tectonic dynamics and correlation of major earthquake sequences of the Xiaojiang and Qujiang-Shiping fault systems, Yunnan, China, *Sci. China Earth Sci.* **41**, 713–724.
- Wills, C. J., M. D. Petersen, W. A. Bryant, M. S. Reichle, G. J. Saucedo, S. S. Tan, G. C. Taylor, and J. A. Treiman (2000). A site-conditions map for California based on geology and shear wave velocity, *Bull. Seismol. Soc. Am.* **90**, S187–S208.
- Xie, F., G. Liu, and H. Liang (1994). Recent tectonic stress field in northwest Yunnan province and its adjacent areas, *Seismol. Geol.* **16**, 329–338.
- Xu, J., H. Zhang, and X. Chen (2015). Rupture phase diagrams for a planar fault in 3-D full-space and half-space, *Geophys. J. Int.* **202**, 2194–2206.
- Yamashita, F., E. Fukuyama, and K. Omura (2004). Estimation of fault strength: Reconstruction of stress before the 1995 Kobe earthquake, *Science* **306**, 261–263.
- Yan, B., S. Toda, and A. Lin (2018). Coulomb stress evolution history as implication on the pattern of strong earthquakes along the

- Xianshuihe-Xiaojijiang fault system, China, *J. Earth Sci.* **29**, 427–440.
- Yang, C. (1982). Temporal and spatial distribution of anomalous ground water changes before the 1975 Haicheng earthquake, *Acta Seismol. Sinica* **4**, 84–89.
- Yoshida, K., A. Hasegawa, T. Saito, Y. Asano, S. Tanaka, K. Sawazaki, Y. Urata, and E. Fukuyama (2016). Stress rotations due to the M6.5 foreshock and M7.3 main shock in the 2016 Kumamoto, SW Japan, earthquake sequence, *Geophys. Res. Lett.* **43**, 10,097–10,104.
- Zhang, S. (1980). The earthquake sequence characteristics of the Tonghai earthquake, January 5, 1970, *J. Seismol. Res.* **2**, 11–18.
- Zhang, S., and B. Liu (1978). Seismic geological characteristics of Tonghai earthquake in 1970, *Sci. Geol. Sin.* **4**, 323–335.
- Zhang, W., and X. Chen (2006). Traction image method for irregular free surface boundaries in finite difference seismic wave simulation, *Geophys. J. Int.* **167**, 337–353.
- Zhang, W., Y. Shen, and X. Chen (2008). Numerical simulation of strong ground motion for the Ms 8.0 Wenchuan earthquake of 12 May 2008, *Sci. China Earth Sci.* **51**, 1673–1682.
- Zhang, Z., and X. Liu (1982). The focal characteristics of the Tonghai earthquake, Yunnan province, on January 5, 1970, *Chin. J. Geophys.* **25**, 440–447.
- Zhang, Z., J. Xu, and X. Chen (2016). The supershear effect of topography on rupture dynamics, *Geophys. Res. Lett.* **43**, 1457–1463.
- Zhang, Z., W. Zhang, and X. Chen (2014). Three-dimensional curved grid finite-difference modelling for non-planar rupture dynamics, *Geophys. J. Int.* **199**, 860–879, doi: [10.1093/gji/ggu308](https://doi.org/10.1093/gji/ggu308).
- Zhang, Z., W. Zhang, X. Chen, P. Li, and C. Fu (2017). Rupture dynamics and ground motion from potential earthquakes around Taiyuan, China, *Bull. Seismol. Soc. Am.* **107**, 1201–1212, doi: [10.1785/0120160239](https://doi.org/10.1785/0120160239).
- Zhou, H., C. R. Allen, and H. Kanamori (1983). Rupture complexity of the 1970 Tonghai and the 1973 Luhuo earthquakes, China, from P-wave inversion, and relationship to surface faulting, *Bull. Seismol. Soc. Am.* **73**, 1585–1597.
- Zhou, R., F. Huang, and Y. Han (1995). The fault plane structure of the Qujiang fault and its seismological implication, *J. Seismol. Res.* **18**, 68–74.
- Zhu, C. (1984). The Qujiang fault geometry and its relation to seismicity, *J. Seismol. Res.* **7**, 525–532.
- Zhu, C. (1985). The Qujiang fault activity in Quaternary period, *Geol. Yunnan* **4**, 178–187.
- Zhu, G., Z. Zhang, J. Wen, W. Zhang, and X. Chen (2013). Preliminary results of strong ground motion simulation for the Lushan earthquake of 20 April 2013, China, *Earthq. Sci.* **26**, nos. 3/4, 191–197.
- Zhu, G., Z. Zhang, W. Zhang, and X. Chen (2016). Simulation of strong ground motion for the Nantou, Taiwan earthquake of 2 June 2013, *Chin. J. Geophys.* **59**, no. 8, 2871–2877.

Manuscript received 18 July 2019
Published online 18 February 2020